An Optical Transport System for Ultracold Dysprosium

A Thesis submitted for the partial completion of
requirements for the degree of

Master of Science
(Research)

by

Nivedith K A
Undergraduate Program
Indian Institute of Science

Under the supervision of

Prof. Dr. Patrick Windpassinger
Institut für Physik, Johannes Gutenberg University, Mainz

Prof. Akshay Singh
Department of Physics, Indian Institute of Science

April 14, 2023

Declaration

I, Nivedith K A, declare that this thesis titled ”Optimising an Optical Transport System for Ultracold Dysprosium” and the work presented in it are my own. I confirm that

1. This work was done wholly while in candidature for the Master of Science (Research) degree at the Indian Institute of Science, Bengaluru.
2. No part of this thesis has previously been submitted for a degree or qualification at any other institution.
3. Whenever I have used materials (data, theoretical analysis, figures, and text) from other sources, I have given due credit to them by citing them in the text of the thesis and giving their details in the references.
4. I have conformed to the norms and guidelines given in the Ethical Code of Conduct of the Institute.

Date: April 14, 2023
Nivedith K A
Undergraduate Program
Indian Institute of Science
Bengaluru, PIN: 560012
nivedithk@iisc.ac.in

Certificate

This is to certify that the Master's thesis entitled "Optimising an Optical Transport System for Ultracold Dysprosium" submitted by Mr Nivedith K A (Sr No: 15784) to the Indian Institute of Science, Bengaluru towards partial fulfilment of requirements for the award of the degree of Master of Science (Research) in Physics is a record of bonafide work carried out by him under my supervision and guidance during Academic Year, 2022-23.

Date: April 14, 2023
Prof. Akshay Singh
Physical Science Department
Indian Institute of Science
Bengaluru, PIN: 560012

Acknowledgements

I wish to express my sincere gratitude to Prof. Dr. Patrick Windpassinger, Institute for Physics, Johannes Gutenberg University, Mainz, for giving me an opportunity to work and gain exposure to cutting-edge research in his. This project would not have been possible without his constant support, encouragement and motivation. I would like to thank Prof. Akshay Singh for agreeing to be my thesis advisor and giving me an opportunity to work in his lab as well as get exposure of working abroad in Mainz, Germany.

I wish to express my immense gratitude to Mr Marvin Proske for guiding me at every step of the project. His constant supervision and support helped me learn and explore the intricate concepts involved in the project and take it forward. I would like to thank my Dy lab colleagues Ishan Varma and Dimitra Cristea for all their help and insightful discussions. I must thank Sören Boles for being the go-to guy for teaching me everything about building vacuum systems and being the go-to guy for solving any problems in the lab. I wish to thank all my colleagues, Malavika, David, Pierre, Esther, Faruk, and Parvez, for their constant support and friendship along the way. I must also thank Elvira and Petra for helping with all the logistical details of my stay in Mainz. I must thank Mr Steffen Hay for being a wonderful landlord and for his constant help throughout my stay at Mainz. I also thank my friends in Aakash, Sudhanshu, Nikhil and Rohan for their amazing company and their delicious biriyanis.

I would also like to thank my OUSUMS labmates in IISc, Hari, Ajit, Mainak, Keerthana and Hardeep, to name a few, for all their help and support.

I thank the UG program and UG physics coordinator Prof. Victor Suvishesha Muthu, for giving us UG students an opportunity to work on cutting-edge research all over the world.

I would like to thank my friends Bazil, Amal, Adithya, Anooj, Dominic, Visalan, both Nikhils, Dhanus etc, for always being there for me. I would also like to thank my batchmates, seniors and juniors who made my undergraduate years wonderful. I would especially like to thank my parents for their constant support and care.

I would also like to thank everyone who helped me in the past five years of my life at IISc.

Abstract

In this thesis, we intend to study light-matter interactions to explore the effects of magnetic dipole-dipole interactions in highly dense samples of atoms exhibiting large permanent magnetic dipole moments. When the average interatomic distances are smaller than the wavelength of the scattering light, strong electric and magnetic dipole-dipole interactions give rise to collective light-scattering phenomena in the spectral and temporal domains. With the largest ground-state magnetic moment in the periodic table (10 Bohr-magneton), dysprosium is the perfect candidate for these experiments. This thesis reports on the progress of generating a dense ultracold dysprosium clouds. For this purpose, we optically transport the atoms to a home built science cell using a high-precision air-bearing translation stage. After achieving such a dense sample, we tune the contact interactions of dysprosium atoms using magnetically tunable Feshbach resonances.

Contents

List of Figures

Chapter 1

Introduction

Spontaneous emission in a gas occurs when the excited atoms are far apart and radiate independently of each other due to weak inter-atomic interactions. These excited atoms emit light isotropically, and emitted light intensity is directly proportional to the number of atoms N in the gas. With decreasing inter-atomic distances, the atoms influence each other more and more, with electric and magnetic dipole-dipole interactions and start emitting coherently in-phase. This leads to a fluorescence intensity proportional to the square of the number of atoms (N^2). Such a coherent emission has a spatial preference of emission along the long axis of the cloud. This anomalous decay mode excited atoms is called "Dicke superradiance" [1, 2]. This phenomenon has been experimentally observed in ultracold gases of Alkali metal species and other Rydberg atoms. But unlike Alkali metals, atoms with permanent dipole moments have long-range anisotropic dipole-dipole interactions. This field of dipolar quantum gases was first explored with the production of Chromium BEC in 2005[3]. In dipolar quantum gases, magnetic dipole-dipole interactions (MDDI) are always much weaker than electric dipole-dipole interactions (EDDI). In such systems, the contact interactions can be tuned using an external magnetic field using Feshbach resonances to enhance the MDDI and enter the strongly dipolar regime[4]. In recent years, lanthanide species with even higher magnetic moments have been condensed, like dysprosium (Dy: 10 μ_B)[5] and erbium (Er: 7 μ_B)[6]. With the largest magnetic dipole moment in the periodic table, Dy is a very interesting candidate for investigating the collective effects by tuning its contact interactions with its rich Feshbach spectrum[7, 8].

1.1 Thesis Outline

In this thesis, a method is presented to prepare dense samples of bosonic dysprosium atoms in an optical dipole trap (ODT). This method involves the optical transport of the dysprosium atoms to a home-built octagonal science cell with a high optical access and numerical aperture to re-trap in a microscopic ODT. Helmholtz surrounds the science cell coils with precise magnetic field control to tune the contact interactions in the highly magnetic Dy atoms.

This thesis is organised as follows. First, a short theoretical overview of Optical dipole traps, collective effects and Feshbach resonances are given in Chapter 2. In Chapter 3, the basic properties of dysprosium, the current experimental setup and the setup of the optical transport system to prepare dense samples of gaseous Dy atoms are discussed. Chapter 4 presents preparing and testing various vacuum epoxies to build the octagonal science cell for the best vacuum. After building the science cell, we move on to the setup, programming and optimisation of the optical transport system in Chapter 5. Chapter 6 discusses the design and characterisation of the Feshbach coil system. In the final chapter, our findings and an outlook on the future of this study into collective effects in Dy atoms are outlined.

Chapter 2

Theory

2.1 Gaussian Beams

Gaussian beams are cardinal in the study of lasers and Optical Dipole Traps (ODT). A Gaussian beam is an EM wave whose transverse amplitude is described by a Gaussian function. These beams retain their Gaussian nature in a homogeneous medium and can be focused into the smallest focal spots[9].
The intensity distribution within a plane perpendicular to the propagation direction is given by

$$\begin{aligned} I(r,z) &= \frac{c\epsilon_0}{2}|\mathcal{A}_0|^2 \left(\frac{w_0}{w(z)}\right)^2 \exp\left(-2\left(\frac{r}{w(z)}\right)^2\right) \\ &= I_0 \exp\left(-2\left(\frac{r}{w(z)}\right)^2\right) \end{aligned} \tag{2.1}$$

Where $\mathcal{A}_0$ is the amplitude of the electric and magnetic field, $w(z)$ is the beam radius at z along the direction of propagation, w_0 is the beam waist, c is the speed of light in vacuum, and ϵ_0 is the permittivity of free space.

The beam radius ($w(z)$) increases with the increase in z, from its smallest value of w_0 at z $= 0$, as shown in figure 2.1.

$$w(z) = w_0\sqrt{1+\left(\frac{z}{z_R}\right)^2} \tag{2.2}$$

The Rayleigh zone of a Gaussian beam is the region around the focus where the beam cross-section area is doubled. In figure 2.1, the Rayleigh length is marked by z_R and has

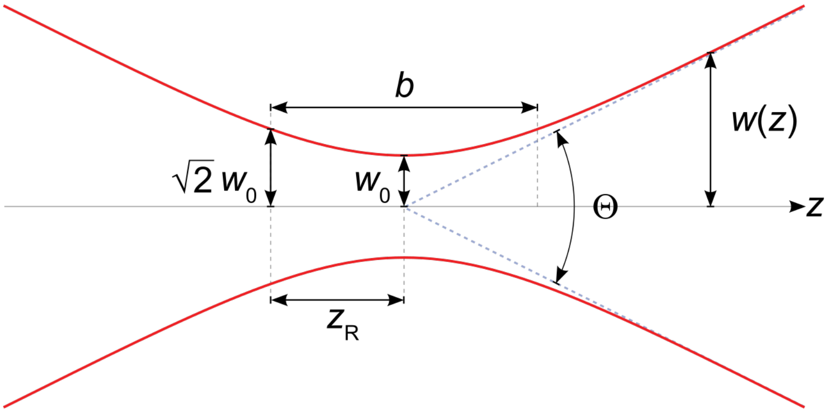

Figure 2.1: Gaussian beam width w(z) as a function of the distance z along the direction of propagation

a beam radius $\sqrt{2}w_0$. For a wavelength λ, Rayleigh length is given by

$$z_R = \frac{\pi w_0^2}{\lambda} \tag{2.3}$$

For a medium with refractive index n, the wavelength is scaled by $\frac{1}{n}$

$$\Rightarrow z_R = \frac{\pi w_0^2}{\lambda/n} = \frac{\pi w_0^2 n}{\lambda} \tag{2.4}$$

2.2 Optical Dipole Trapping

In this section, we derive the expression for the trapping potential of an optical dipole trap of a focussed a Gaussian beam. This section follows the discussion in [10]. Initially, we consider a semi-classical model of an atom in a light field to model the optical dipole interaction. This semi-classical Oscillator model assumes a classical light field and a quantum two-level system as the atom.

2.2.1 Oscillator model

Consider an atom placed in a laser field that produces an electric field $\vec{E}(\vec{r},t) = \hat{e}\tilde{E}(\vec{r})\exp\{-i\omega t\} + c.c.$, which induces an electric dipole moment $\vec{p}$ given by

$$\vec{p}(\vec{r},t) = \hat{e}\tilde{p}(\vec{r})\exp\{-i\omega t\} + c.c. \tag{2.5}$$

where, $\hat{e}$ is the unit polarization vector and $\tilde{p}$ is related to the electric field by $\tilde{p} = \alpha(\omega)\tilde{E}$. The interaction potential of the induced dipole moment $\vec{p}$ in the Electric field is given by

$$\begin{aligned} U_{dip} &= -\frac{1}{2}\left\langle \vec{p}.\vec{E} \right\rangle \\ &= -\frac{1}{2\epsilon_0 c}\,\mathrm{Re}(\alpha) I \end{aligned} \tag{2.6}$$

where I stands for the intensity of the field related to the electric field amplitude by $I = 2\epsilon_0 c\left|\tilde{E}\right|^2$.

The dipole force is given by the negative gradient of the dipole potential

$$\begin{aligned} \vec{F}_{dip} &= -\nabla U_{dip}(\vec{r}) \\ &= \frac{1}{2\epsilon_0 c}\,\mathrm{Re}(\alpha)\nabla I(\vec{r}) \end{aligned} \tag{2.7}$$

$\vec{F}_{dip}$ is a conservative force because $\nabla \times \vec{F}_{dip} = 0$.

The average power absorbed by the oscillator from the electric field is given by

$$\begin{aligned} P_{abs} &= \left\langle \dot{\vec{p}}.\vec{E} \right\rangle \\ &= 2\omega\,\mathrm{Im}(\tilde{p}\tilde{E}^*) \\ &= \frac{\omega}{\epsilon_0 c}\,\mathrm{Im}(\omega) I(\vec{r}) \end{aligned} \tag{2.8}$$

Considering the light as a stream of photons of energy $\hbar\omega$, the scattering rate as the ratio of P_{abs} to the energy of one photon can be written as

$$\Gamma_{sc}(\vec{r}) = \frac{1}{\hbar\epsilon_0 c}\,\mathrm{Im}(\alpha) I(\vec{r}) \tag{2.9}$$

The dipole potential and scattering rate completely characterise a dipole trap. These two quantities are functions of field intensity $I(\vec{r})$ and the polarizability $\alpha(\omega)$. We can use Lorentz's model of a classical oscillator for an atom to derive an expression of the polarizability α. This model considers an electron bound to the nucleus with an optical transition frequency ω_0. The dipole radiation provides a damping force according to the Larmor formula for an accelerating charge. The resulting equation of motion is given by

$$\ddot{x} + \Gamma_\omega \dot{x} + \omega_0^2 x = -\frac{eE(t)}{m_e} \tag{2.10}$$

We can calculate the polarizability by solving the above equation motion to get

$$\alpha = 6\pi\epsilon_0 c^3 \frac{\Gamma/\omega_0^2}{\omega_0^2 - \omega^2 - i(\omega^3/\omega^2)\Gamma} \tag{2.11}$$

For far-detuned values of ω, the scattering rate becomes low enough for heating effects to be negligible. In this case, we can write the following expressions

$$U_{dip}(\vec{r}) = -\tfrac{3\pi c^2\Gamma}{2\omega_0^2}\left(\tfrac{1}{\omega_0-\omega}+\tfrac{1}{\omega_0+\omega}\right)I(\vec{r}) \tag{2.12}$$

$$\Gamma_{sc}(\vec{r}) = \tfrac{3\pi c^2\Gamma^2}{2\hbar\omega_0^3}\left(\tfrac{\omega}{\omega_0}\right)^3\left(\tfrac{1}{\omega_0-\omega}+\tfrac{1}{\omega_0+\omega}\right)^2 I(\vec{r}) \tag{2.13}$$

In most experiments, we choose the ω to be such that $\Delta \equiv \omega - \omega_0 \ll \omega_0$. This helps us approximate the equations 2.12 and 2.13 as

$$U_{dip}(\vec{r}) = \tfrac{3\pi c^2}{2\omega_0^3}\tfrac{\Gamma}{\Delta}I(\vec{r}) \tag{2.14}$$

$$\Gamma_{sc}(\vec{r}) = \tfrac{3\pi c^2}{2\hbar\omega_0^3}\left(\tfrac{\Gamma}{\Delta}\right)^2 I(\vec{r}) \tag{2.15}$$

The above equations show that the dipole potential is attractive when $\Delta < 0$; this is called red detuning. The other case is when $\Delta > 0$, referred to as blue detuning, is repulsive.

The dipole trapping potential U_{dip} scales as $\frac{I}{\Delta}$ while the scattering rate scales as $\frac{I}{\Delta^2}$. So, we use optical dipole traps using large detunings and high intensities to keep the scattering rate as low as possible at a certain potential depth.

2.2.2 AC Stark Effect

In the semi-classical oscillator model, we do not account for the shift in the energy levels of the atoms due to varying electric fields due to the laser. This shift in energy levels of an atom is called the Stark effect. The effect of far-detuned laser light on the atomic levels can be treated as a perturbation in the second order of the electric field given by

$$\Delta E_i = \sum_{j\neq i}\frac{\left|\langle j|\mathcal{H}_1|i\rangle\right|}{\varepsilon_i - \varepsilon_j} \tag{2.16}$$

where, the dipole interaction Hamiltonian $\mathcal{H}_1 = -\hat{\mu}.\vec{E}$ with $\hat{\mu} = -e\vec{r}$

In its ground state, the atom has zero internal energy, and the field with n photons has an energy $n\hbar\omega$. When the atom absorbs a single photon from the field and moves into the excited state, the sum of the total energy of the atom and the field becomes $\varepsilon_j = \hbar\omega_0 + (n-1)\hbar\omega = -\hbar\Delta_{ij} + n\hbar\omega$. For a two-level system, we can write 2.16 as

$$\Delta E = \pm\frac{\left|\langle e|\mu|g\rangle\right|^2}{\Delta}|E|^2 = \pm\frac{3\pi c^2}{2\omega_0^2}\frac{\Gamma}{\Delta}I \tag{2.17}$$

where, $I = 2\epsilon_0 c\left|\tilde{E}\right|^2$.

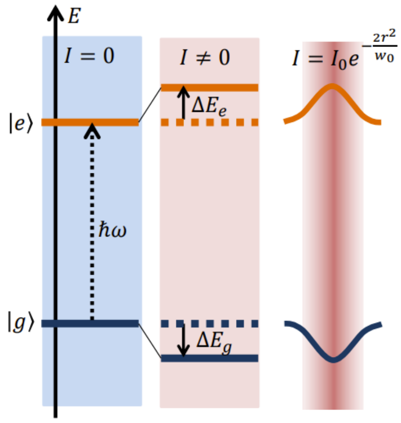

Figure 2.2: Light shift for a two-level atom for a red-detuned light. The right-hand side shows the effect of a spatially inhomogeneous field like a Gaussian beam that produces a ground state potential well[11]

The optically induced or AC stark shift moves the ground state and excited states away from each other according to the intensity of the laser. As shown in figure 2.2, for Gaussian beams, the shift is shaped like a potential well in which an atom can be trapped.

2.2.3 Trap frequencies

Trap frequencies are an important factor that characterises an ODT; it is determined by the geometry of the irradiated laser beam, its power and the atoms trapped. An elliptical beam is considered because a circular beam is only sometimes realisable in practice. For an elliptical Gaussian beam with beam waists $w_{0,x}(z)$ and $w_{0,y}(z)$ along x and y directions respectively, we can write the intensity distribution as

$$I(\vec{r} = (x, y), z) = \frac{2P_0}{\pi w_{0,x}(z) w_{0,y}(z)} \exp\left\{-2\left(\frac{x^2}{w_{0,x}^2(z)} + \frac{y^2}{w_{0,y}^2(z)}\right)\right\} \tag{2.18}$$

From the expression for dipole trapping potential in 2.14, we can write $U_{dip} = U_0 I(\vec{r})$ where, $U_0 = \frac{3\pi c^2}{2\omega_0^3}\frac{\Gamma}{\Delta}$. For small values of x and y, we can use series expansion to the second order to approximate the trapping potential as harmonic.

$$U_{dip} \approx U_0 \left[1 - \frac{2x^2}{w_x^2} - \frac{2y^2}{w_y^2} - \frac{1}{2}x^2(z_{R_x}^{-2} + z_{R_y}^{-2})\right] \tag{2.19}$$

Comparing this to a standard harmonic oscillator, we get

$$\omega_x \equiv \sqrt{\frac{4U_0}{m w_x^2}}, \omega_y \equiv \sqrt{\frac{4U_0}{m w_y^2}}, \omega_x \equiv \sqrt{\frac{2U_0}{m z_{R_{ell}}^2}} \tag{2.20}$$

where, $z_{R_{ell}}$ a quantity we define as $z_{R_{ell}} \equiv \frac{z_{R_x} z_{R_y}}{\sqrt{\frac{1}{2}(z_{R_x}^2 + z_{R_y}^2)}}$
These trapping frequencies indicate the depth of the trap in each direction.

2.3 Feshbach Resonances

A Feshbach resonance occurs when two slow-moving atoms collide to temporarily form an unstable bound state. During such a scattering process, the kinetic energy of the incoming atoms must be equal to the inter-atomic potential. Experimentally we are interested in tuning the strength of such interactions by controlling the magnetic field to study molecular bound states of Dy atoms. This section discusses the basic theory of Feshbach resonances using molecular potential curves[12, 13].

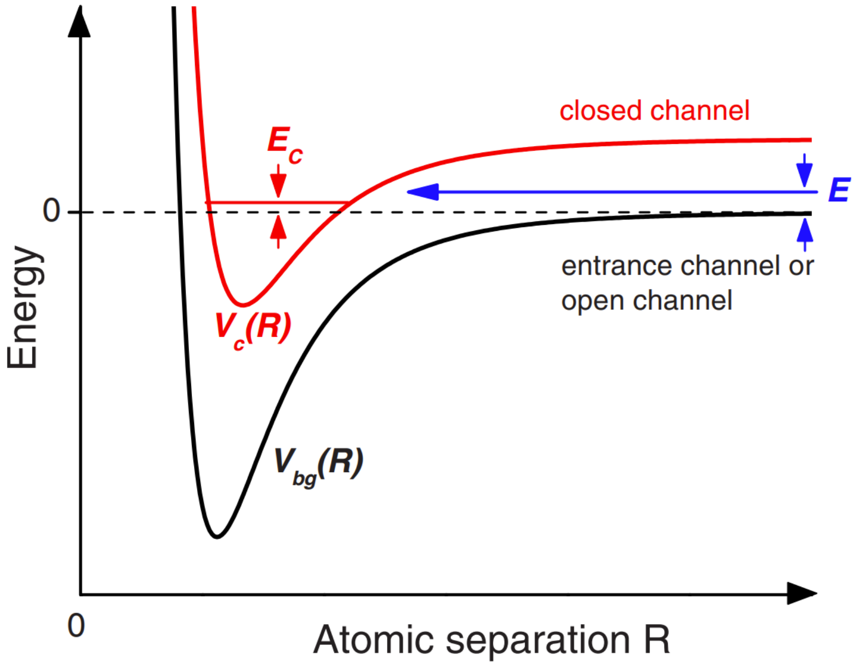

Figure 2.3: A basic two-channel model for a Feshbach resonance[12]

Consider two molecular potential curves $V_{bg}(R)$ and $V_c(R)$ as shown in figure 2.3. Here, $V_{bg}(R)$ represents the background potential that connects any two free atoms in a cold atom gas. Due to the extremely low kinetic energy of atoms in such a cold gas, we assume that they enter very close to the dissociation threshold. However, they cannot separate once they are close enough to the molecular bound state supported by the conservation of energy as indicated by the closed channel curve $V_c(R)$. A Feshbach resonance occurs when the bound molecular state in the closed channel energetically approaches the scattering state in the open channel. The energy of the scattering state can be altered using Zeeman energy level shifts controlled by an external magnetic field.

2.3.1 Magnetically Tunable Feshbach Resonances

For magnetic atomic species, an external magnetic field can be used to shift the energy levels in the atoms, which changes the contact interactions. The Zeeman effect due to the external magnetic field can alter the value of E_c by shifting the closed channel hence altering the mixing between the two channels. A magnetically tuned Feshbach resonance for s-wave scattering length a can be expressed as a function of magnetic field B[14].

$$a(B) = a_{bg}\left(1 - \frac{\Delta}{B - B_0}\right) \tag{2.21}$$

where, B_0 represents the resonance position, a_{bg} is the background scattering length and Δ is the resonance width.
A particular magnetic field value B_0 is a Feshbach resonance when $a(B = B_0)$ diverges i.e. $a \longrightarrow \pm\infty$ as shown in figure 2.4. In addition, the resonance width Δ is determined by the zero crossing of $a(B)$ at $B = B_0 + \Delta$ In the above figure 2.4, we can see that the

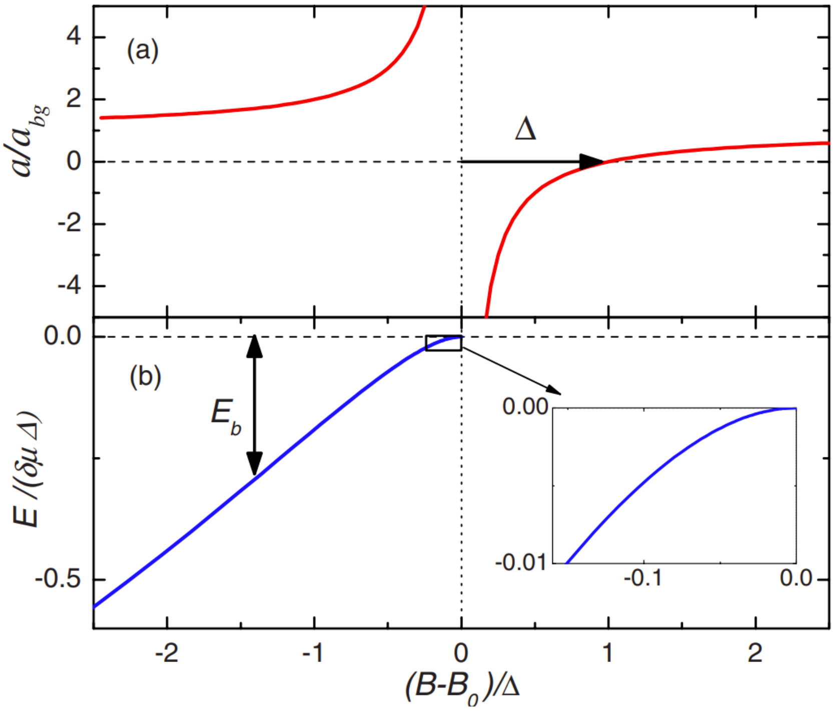

Figure 2.4: Scattering length of a Magnetically tuned Feshbach Resonance[12]

binding energy E_b moves towards zero as we approach B_0. As we move very close to B_0

from the $B < B_0$ side, we can write

$$E_b \approx \frac{\hbar^2}{2\mu a^2} \tag{2.22}$$

where, μ is the reduced mass of the atom pair and a is scattering length determined from equation 2.21.

2.3.2 Feshbach Resonances in Dysprosium

In highly dipolar species like Dysprosium, anisotropic magnetic dipole-dipole interactions (MDDI) are responsible for giving rise to a plethora of many-body interactions[8]. But the magnitude of MDDI is just a perturbation compared to the electric dipole-dipole interactions[4]. The relative strength of MDDI compared to EDDI is inversely proportional to the scattering length a. The magnetically tunable Feshbach resonances allow us to tune the value of a and investigate the effects of stronger dipolar effects.

To effectively tune the Feshbach resonance of Dysprosium, we need a very stable magnetic field source with a high resolution and low noise. A typical width of a Feshbach resonance peak in the order of 5 mG [15, 16]. But there are larger resonances with a width greater than 1 G, as shown in figure 2.5.

Hence, the magnetic field system should have a low noise to resolve the smaller resonances.

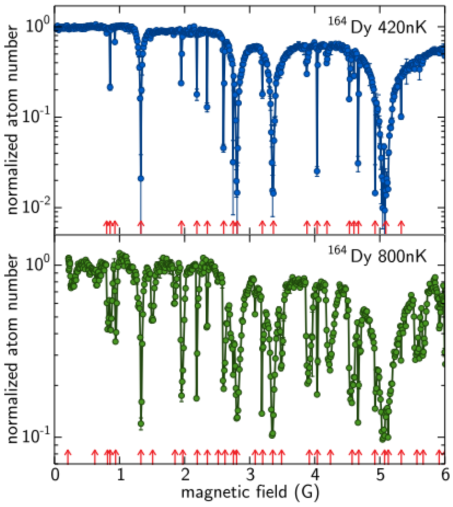

Figure 2.5: Feshbach resonances of Dy[17]

Chapter 3

Setup of the Dysprosium Experiment

This chapter describes the existing setup to cool and trap dysprosium atoms. First, the important properties of dysprosium are discussed. Then the existing cooling mechanism and experimental setup are outlined. Lastly, a plan to expand the experimental setup to prepare much denser atomic samples is described.

3.1 Dysprosium

Dysprosium is an element in the lanthanide group with an atomic number of 66. The ground state electron configuration is $[\mathrm{Xe}]4\,\mathrm{f}^{10}\,6\,\mathrm{s}^2$. Important isotopes of Dy are listed in table 3.1. Due to the four unpaired electrons in the f orbital, Dy has a total spin of S = 2, a total orbital angular momentum of L = 6 and a total angular momentum of J = 8. This work focuses on the ^{164}Dy isotope.

Dysprosium is particularly interesting because of its large magnetic dipole moment of $\mu = 10\mu_B$, the highest in the periodic table. This gives rise to strong dipole-dipole interactions, which are a hundred times stronger than in alkali metals ($\approx 1\mu_B$). The

Isotope	Abundance	Nuclear Spin	Statistics
^{160}Dy	2.34%	0	Boson
^{161}Dy	18.9%	5/2	Fermion
^{162}Dy	25.5%	0	Boson
^{163}Dy	24.9%	5/2	Fermion
^{164}Dy	28.2%	0	Boson

Table 3.1: Stable Isotopes of Dysprosium and their natural abundances

dipole-dipole interaction energy for two dipoles aligned along $\hat{e}_1$ and $\hat{e}_2$ is given by[18]

$$U_{dd} = \frac{\mu_0 \mu^2}{4\pi} \frac{(\hat{e}_1.\hat{e}_2)r^2 - 3(\hat{e}_1.\vec{r})(\hat{e}_2.\vec{r})}{r^5} \tag{3.1}$$

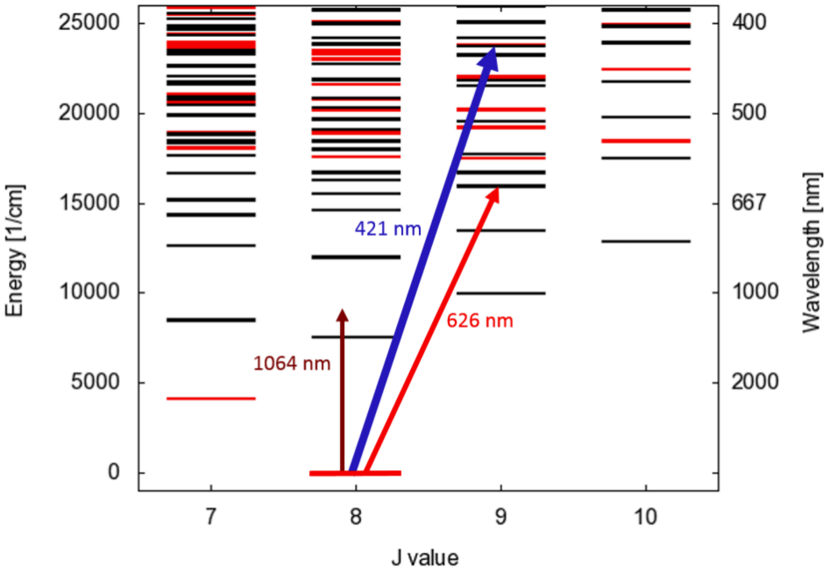

Figure 3.1: Energy levels of dysprosium isotope used with odd parity states in black and even in red. Selection rules only allow transitions from the even red states to odd excited states

The electronic energy level diagram of ^{164}Dy isotope is shown in figure 3.1. The three transitions we use for our experiment are marked in the diagram, and their properties are given in table 3.2.

Line	$\Gamma/2\pi$	I_{Sat}	$T_{Doppler}$
421 nm	32.2 MHz	56.4 mW$/cm^2$	774 μK
626 nm	136 kHz	72 $\mu W/cm^2$	3.2 μK

Table 3.2: Cooling Transitions used for dysprosium

3.2 Current Experimental Setup

We create a stream of dysprosium atoms by heating it to 1250°C in an effusion cell. This ejected stream of atoms is slowed down and trapped in three steps. We will briefly explore these three steps in the following sections.

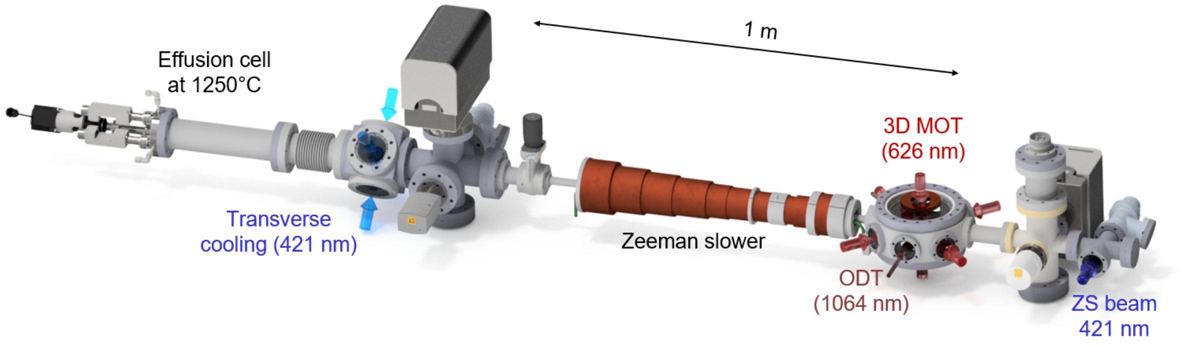

Figure 3.2: Experimental setup to cool and trap dysprosium atoms

3.2.1 Transversal Cooling

The first step in the cooling process is collating the atoms in a single direction by restricting transverse velocity to increase the number of atoms reaching the MOT chamber. The atoms ejected in the effusion cell move and exhibited an isotropic velocity distribution in all directions. Transversal cooling involves using 2D molasses of a red-detuned laser to reduce the velocity components perpendicular to the axis of the experimental setup. A red-detuned laser is used because the energy of the photon observed by the atom changes depending on its speed and direction due to the Doppler effect. Therefore, a slightly red-detuned photon blue shifts for an atom moving towards it and reduces its speed upon absorption. As shown in figure 3.2, we have four beams of 421 nm laser perpendicular to each other to achieve the transversal cooling and increase the flux of atoms in the direction of the main chamber of the experiment.

3.2.2 Zeeman Slower

After transversal cooling, the atoms have a speed of about 450 m/s in the direction of the main chamber[19]. In the next step, we reduce the longitudinal velocity of the atoms by exploiting the Zeeman effect in the atoms. In the setup, a circularly polarised 421 nm red detuned laser is irradiated against the direction of the flow of atoms, and a magnetic field is used to vary the energy levels in the atoms. Due to the continuous momentum transfer due to the collision with 421 nm photons, the average speed of atoms decreases as they move forward. Due to the Doppler effect, this puts it out of resonance with the red-detuned 421 nm laser. We use the Zeeman slower coils to reduce the magnetic field along the longitudinal direction linearly. The value of the magnetic field is set such that the atoms are pushed back into resonance with the laser as the speed decreases along the Zeeman slower. This kind of magnetic field distribution is achieved by reducing the number of windings along the Zeeman slower. This continuous reduction in the longitudinal velocity of the atoms in the Zeeman slower decelerates the atoms up to 20 m/s[19].

3.2.3 Magneto-optical Trap

A Magneto-Optical Trap (MOT) traps and confines the atoms in a particular region in space. Such confinement is achieved using three sets of counter-propagating circularly polarised beams of opposite polarity in mutually perpendicular directions and two coils in an anti-Helmholtz configuration. The anti-Helmholtz coils produce a uniform magnetic field gradient along the z direction, which produces a half-strong gradient in the other two directions. This is due to Maxwell's equation $\nabla.\vec{B} = 0$ which leads to $\partial_x B_x = \partial_y B_y = \frac{1}{2}\partial_z B_z$ due to symmetry.

Our experimental setup uses a 626 nm laser corresponding to $m_J = 8$ to $m_{J\prime} = 9$ transition in dysprosium. The magnetic field gradient produces a position-dependent Zeeman shift with a zero shift at the centre of the MOT. Such a magnetic field and the circularly polarised beams excite only the atoms moving away from the centre, providing a recoil force that holds atoms in the cloud.

Due to the very low linewidth of 626 nm transition of 136 kHz in Dy, the MOT cools and traps the atoms near the Doppler temperature of 3.3 μK. These atoms are then transferred to an Optical Dipole Trap to achieve higher densities.

3.2.4 Beam Path Transport Beam

A Mephisto MOPA produces the 1064 nm laser from Coherent Inc with a maximum power of 42 W. A sketch of the setup is given in figure 3.3." The Mephisto outputs 42

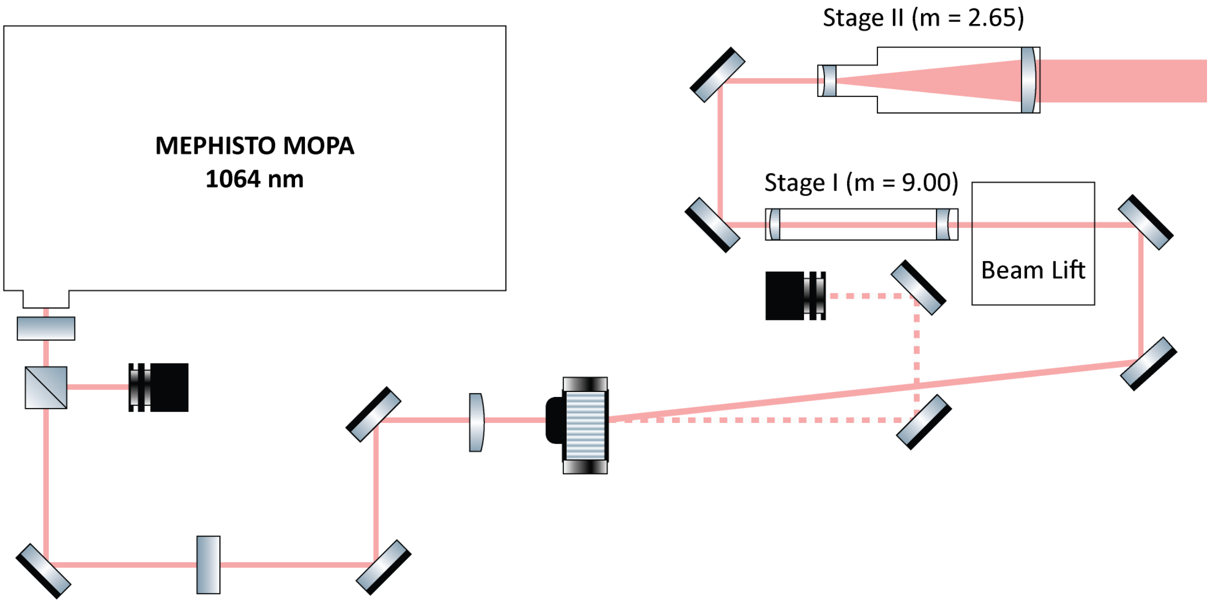

Figure 3.3: Path of 1064 nm laser from Mephisto laser

W of linearly polarised 1064 nm laser with a diameter of 1.2 mm. A half-wave plate (HWP) and a polarising beam splitter (PBS) control the power output. The beam is then collimated using a convex lens and directed into an acousto-optic modulator (AOM). The AOM is used as a switch by directing the zeroth order into a beam dump and only using the first order for the experiment. The laser beam is then shifted vertically by a set of mirrors acting like a beam lift to match the height of the MOT chamber windows. Now the beam is expanded in two stages by a telescope arrangement of lenses. In stage one, the beam is expanded using a telescope of magnification 9 to increase the diameter from 1.2 mm to 10.8 mm. Next, stage two expands the diameter from 10.8 mm to 28.6 mm using a magnification of 2.65.

An optical dipole trap directly in the MOT chamber is restricted by the low optical access and low numerical aperture (NA), as shown in figure 3.4. This large working distance of 135 mm restricts us from reaching the densities required to observe collective effects.

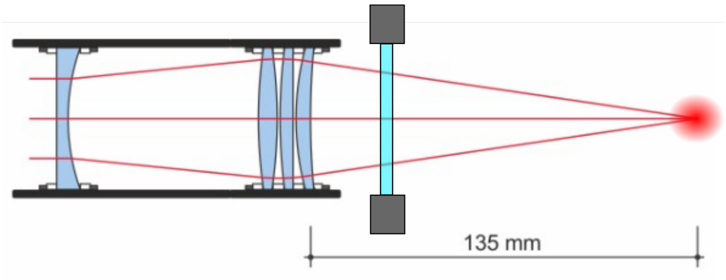

Figure 3.4: ODT at the centre of the MOT chamber

To circumvent this issue, we build a science cell (4.1) with seven windows and a width of just 40 mm to achieve a very high NA of 0.65 and additional optical access. We have to transport the atoms from the centre of the MOT chamber to the centre of the science cell. These transported atoms are then re-trapped in a tightly focused microscopic ODT, which is expected to provide up to 10^{14} atoms/cm^3. A detailed description of the characterisation of this ODT objective can be found in [20].

3.3 Optical Transport System

A high-precision air-bearing translation stage transports optically dysprosium atoms from the MOT chamber to the Science Cell. Our experiment uses Aerotech ABL1500-300 stage with a 300 mm movement range for transport. It has an accuracy of $\pm 0.5\mu$m and repeatability of $\pm 0.15\mu$m. It has a maximum speed of 2 ms^{-1} and a maximum acceleration of 2g.

3.3.1 Transport Setup

First, an achromatic lens with a 750 mm focal length focuses down the 1064 nm beam at the MOT position. The focusing beam is directed using two mirrors mounted on the translation stage. When the translation stage is moved backwards, the focal spot inside the MOT chamber moves towards the centre of the Science Cell. After the transport, the atoms are re-trapped in a new, tightly focused microtrap objective.

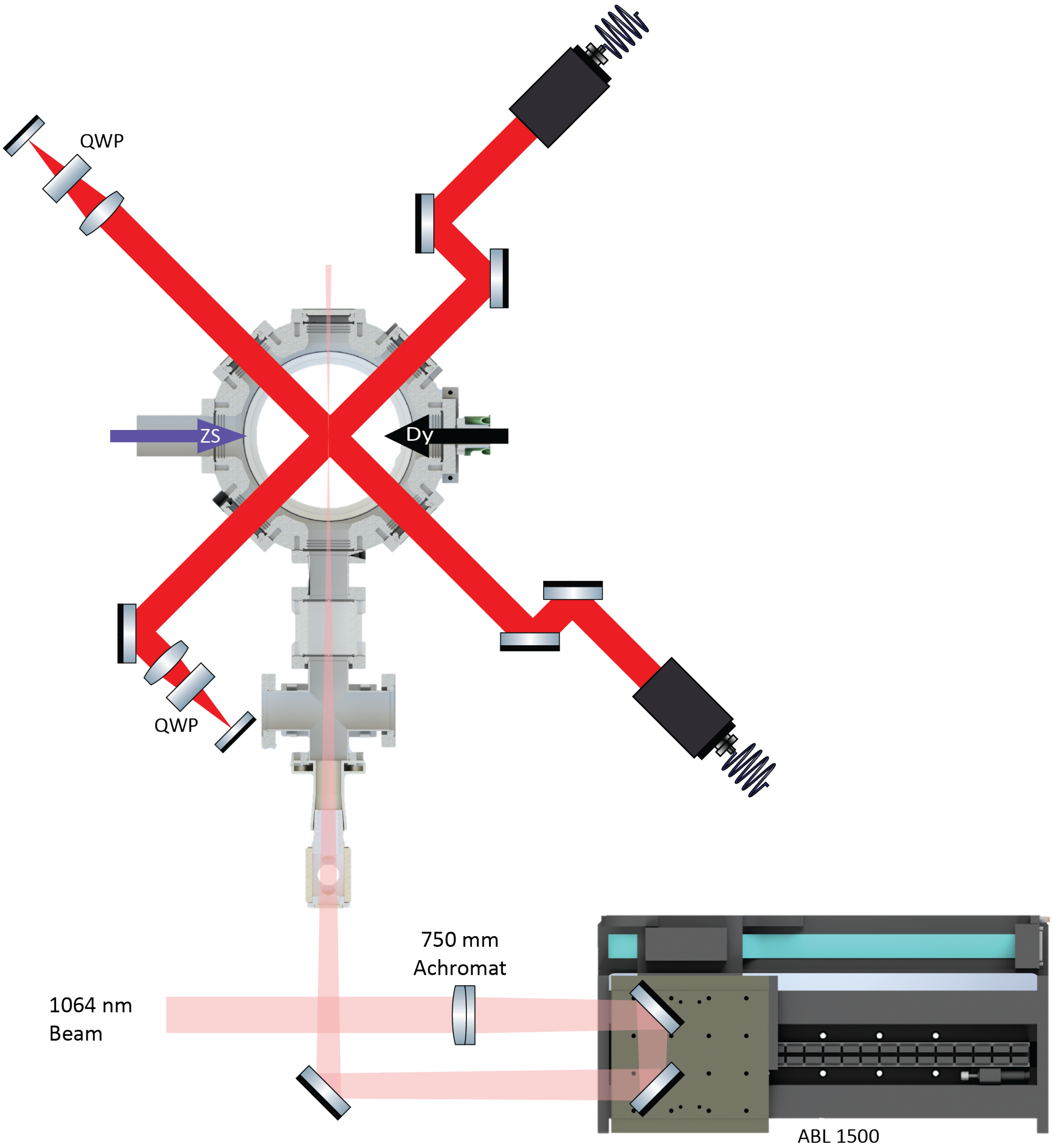

Figure 3.5: ABL1500 stage before transport, ODT inside the MOT chamber. During the transport the translation stage moves to the right and drags the atoms in the MOT chamber to the science cell over a distance of 32 cm

Chapter 4

Science Cell

A vacuum environment in the order of 10^{-10} mbar is needed for our experiments to reduce the atoms confined in the optical dipole trap from heating up due to collisions from the background gas and leaving the trap. This chapter discusses the vacuum testing and preparation of the science cell. Science Cell is an octagonal Macor ceramic cell with two big windows opposite each other and seven small windows arranged on the sides of an octagon. The last one extends out as a conical connector inserted into a Titanium flange. All the windows are glued on ceramic with epoxies that can handle ultra-high vacuums. The windows are made of UV-fused silica to withstand high temperatures and high-intensity laser beams and are also coated with Anti-Reflection coatings for 421 nm, 626 nm and 1064 nm. In this chapter, we discuss the test of various epoxies to determine the best one to make the window-ceramic and ceramic-titanium flange connections for the best vacuum conditions.

Due to a Non-Disclosure Agreement, the exact names of the epoxies that are tested cannot be disclosed in this thesis. So the three epoxies considered for the construction of

Figure 4.1: Science Cell

the science cell will be referred to as A, B and C. Epoxies A and C are NASA-approved low-outgassing sealants. The epoxies are applied using a syringe to the gap between the window and the ceramic while being slowly rotated on a stage. The entire setup is then cured at a high temperature.

A test cell was designed to test various epoxy combinations for ceramic-window and ceramic-flange sealing. A test has only a single window and conical connector. This allows us to test a single epoxy to select the best-performing one without wasting a lot of Macor and multiple UV-fused silica windows.

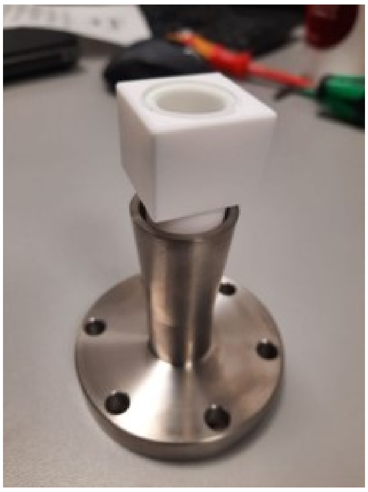

Figure 4.2: A test cell

4.1 Creeping Tests

First, the creeping behaviour of the epoxies below the windows is investigated. It is important that the epoxies don't creep below the windows and block the optical access to the science cell. The results of the creeping test of the three epoxies are shown in figure 4.3 in the order A, B and C.

We can see that epoxy C has crept below the window and has blocked a part of the window. So, epoxy C is rejected for further testing.

4.2 Vacuum Testing

The next step is to prepare the test cells with various epoxy combinations for the window-ceramic and ceramic-flange sealing and test if it can reach ultrahigh vacuum near 10^{-10} mbar. For this, we first check Helium leakage performance and then measure the maximum vacuum it can reach.

Figure 4.3: Creeping test results of the three epoxies

A simple way to investigate the leakage rates of a vacuum cell is to use a helium leakage seeker. It consists of a vacuum pump in combination with a mass spectrometer. During the test, the test cell is connected to the leakage seeker, which evacuates the cell using a pre-pump and a turbomolecular pump. Then Helium gas is sprayed on top of the test cell using a nozzle. The mass spectrometer in the leakage seeker detects the amount of Helium gas leaking into the cell and calculates the leakage rate. We use Agilent HLD leak detector with a sensitivity of 5×10^{-12} mbar.L/s with a minimum detection of 10^{-11} mbar.L/s.

After measuring the helium leakage rates of the test cells, a pre-pump, a turbo-pump and an Ion pump are used to create the vacuum as shown in figure 4.4.

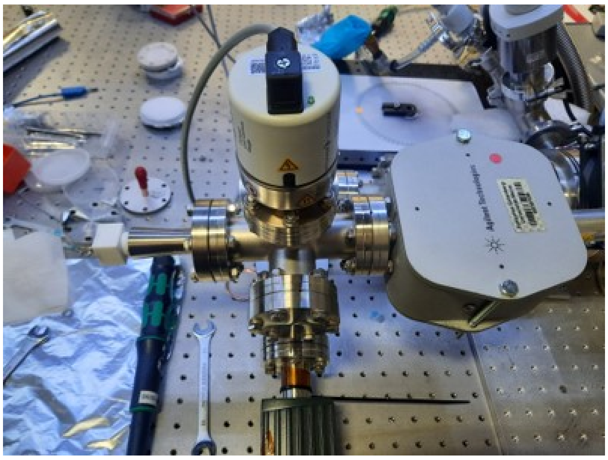

Figure 4.4: Vacuum Testing Setup

There are four possible combinations of applying the epoxies A and B to the window and flange: A-A, B-B, A-B and B-A. Both epoxies are cured at 150°C for one hour at 1°C per minute heating up and an average of 0.6°C per minute cooling down. The results of helium leakage tests and the best vacuum obtained for these four combinations are given in table 4.1.

The test cells prepared with epoxies cured at 150°C show very high leakage rates and

Window-Flange Epoxies	Helium Leakage Rates	Best Final Pressure
A-A	$\geq 10^{-6}$ mbarL/s	$1.6 \times 10^{-9} mbar$
A-B	$\geq 10^{-3}$ mbarL/s	$1.9 \times 10^{-9} mbar$
B-A	$\geq 10^{-3}$ mbarL/s	N/A
B-B	$\geq 10^{-3}$ mbarL/s	N/A

Table 4.1: Performance of Test cells with epoxies cured at 150°C

exhibit a sudden increase in pressure after it reaches the highest vacuum after baking out. This could be due to the formation of microscopic cracks in the epoxies due to the high rate of cooling down after curing and baking out the system. So, in an attempt to improve the performance of the epoxies, they are cured and baked out at a lower temperature for a longer time. The next batch of epoxies is cured at 80°C for 640 minutes with a temperature ramp of 0.25°C. In addition, the epoxies are initially kept in an ultrasonic bath to prevent bubbles from remaining inside the bulk and getting trapped inside the epoxy after curing. The results of this method of test cell preparation are given in 4.2.

The helium leakage rates obtained for these combinations are $\leq 10^{-11}$ mbarL/s; this means that the leakage is lesser than the detection limit of the Agilent Helium leakage seeker. At the time of writing the thesis, the vacuum measurement of B-B is in progress. Since the Helium leakage rate is below the detection level, we go ahead with these two epoxy combinations for the assembly of the octagonal science cell.

Window-Flange Epoxies	Helium Leakage Rates	Best Final Pressure
A-A	$\leq 10^{-11}$ mbarL/s	5.28×10^{-10} mbar
B-B	$\leq 10^{-11}$ mbarL/s	TBM

Table 4.2: Performance of Test cells with epoxies cured at 80°C

Chapter 5

Transport System

In the previous chapter, the construction of the science cell was discussed. This chapter discusses the setting up and the optimisation of the transport system to the science cell. Atom transport can be achieved using multiple methods like optical conveyer belts [21, 22], focus tunable lenses[23] and translation stages [24]. This experiment uses a high-precision air-bearing translation stage because of its high repeatability, long translation range and higher transport efficiency.

5.1 Transport Beam Characterization

For the transport of atoms from the MOT chamber to the science cell, Mephisto MOPA single-mode solid-state 1064 nm laser is used. Measuring the diameter of this beam is crucial because it is one of the factors that determines the focal spot size of the beam other than the lens that focuses it.

5.1.1 Knife Edge Measurements

Knife Edge Measurements involve blocking a part of the beam with a sharp edge and measuring the power of the rest. Assuming the beam is Gaussian, the resulting power plotted against the distance plot should be an error function. This error function fully characterises the power distribution of the underlying Gaussian beam. Here we perform a knife-edge measurement of the 1064 nm after the stage II telescope to measure the beam diameter in the horizontal and vertical directions. The measurement results are plotted in 5.1 and 5.2. The error function fit gives the vertical beam size (4σ) 20.85 ± 0.15 mm and the horizontal beam size 28.91 ± 0.16 mm. This clearly indicates that the beam is slightly elliptical.

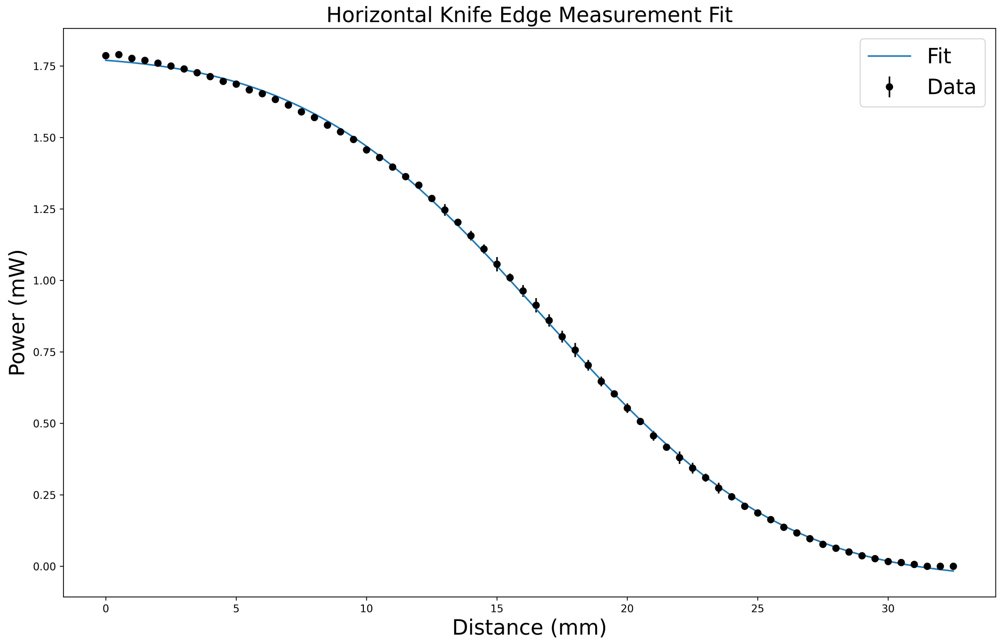

Figure 5.1: Horizontal Knife Edge Measurement of 1064 nm beam

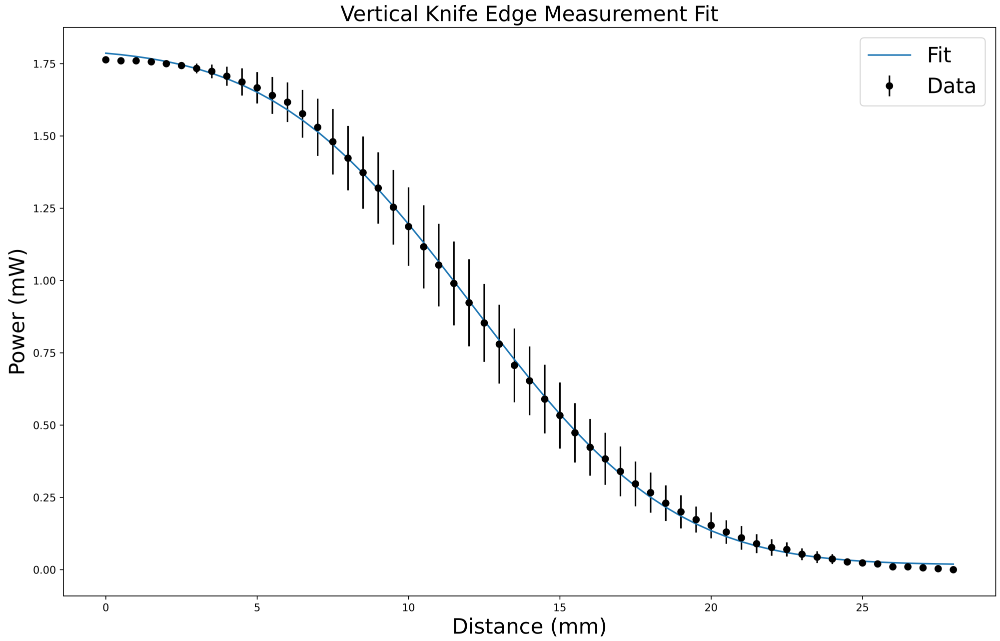

Figure 5.2: Vertical Knife Edge Measurement of 1064 nm beam

5.2 Achromat Characterization

The next step is characterising the focal spot size of 750 mm achromat produced by the 1064 nm beam. The focal spot size is an important parameter determining the trap depth and trap frequencies of the transport ODT. A piezo element with μm precision is used to perform the knife-edge measurements near the focal spot, as shown in figure 5.3. Multiple knife-edge measurements are carried out near the focal spot to find the minimum beam size to determine the focal spot precisely.

The results of Knife edge measurements of the focal spot of the achromatic lens are plotted in 5.4, which gives the focal spot size to be approximately 66 μm.

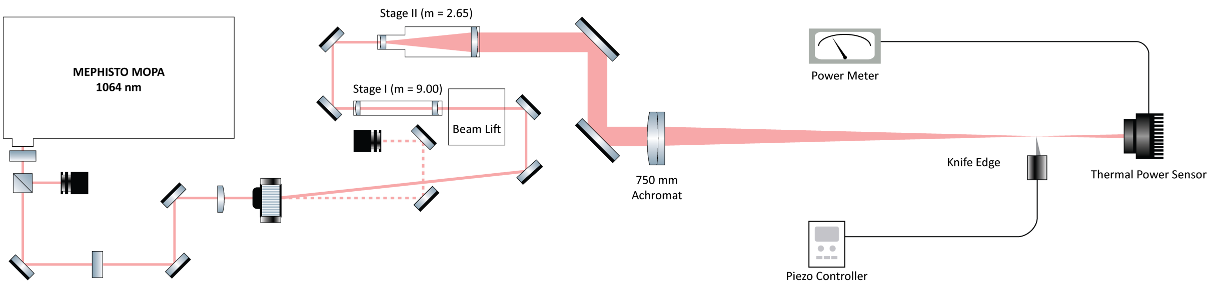

Figure 5.3: Knife Edge Measurement Setup for 750 mm achromatic lens

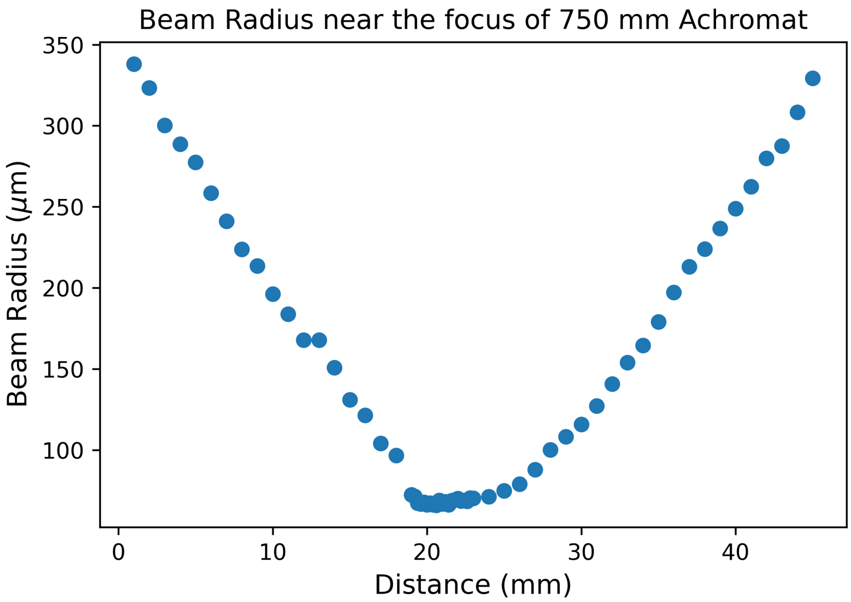

Figure 5.4: Beam radius near the focus of the 750 mm achromatic lens from the knife edge measurements

5.3 Programming the triggered real-time system for Transport

A LabVIEW program that controls the Adwin system coordinates the cooling and trapping of Dy atoms. This experimental control program triggers all the experimental components in a real-time fashion to reduce the shot-to-shot variation. A real-time system implements any task in a fixed amount of time[25]. This kind of timed operation is essential in cold atom experiments due to the short lifetime of atoms in traps.

The transport with the stage must be integrated into the existing system and triggerable using Adwin. The ABL1500 stage is programmed using its Aerotech Aeroscript code and loaded into the controller. A simplified flowchart of the operation is shown in figure 5.5.

The main experimental control program controls the Adwin system and loads the Aeroscript code into the iXC2 controller of the ABL1500 stage. It first reads for the motion parameters given by the user and moves the stage to the starting position. The Aeroscript checks for a trigger signal in the digital port of the iXC2 controller every 3 ms. So, the stage trigger duration is set to 4 ms from the Adwin system. Once the iXC2 controller detects a trigger signal, it waits 45 ms before starting the motion every time. This makes it a timed real-time system[25]. After the motion is completed, the position and speed values of the stage during the motion are stored, and the stage is moved back into the starting position. To optimise the transport parameters, a feature is implemented in the program to change the motion settings on the go without restarting the program. While the new motion parameters are loaded, the system can take up to

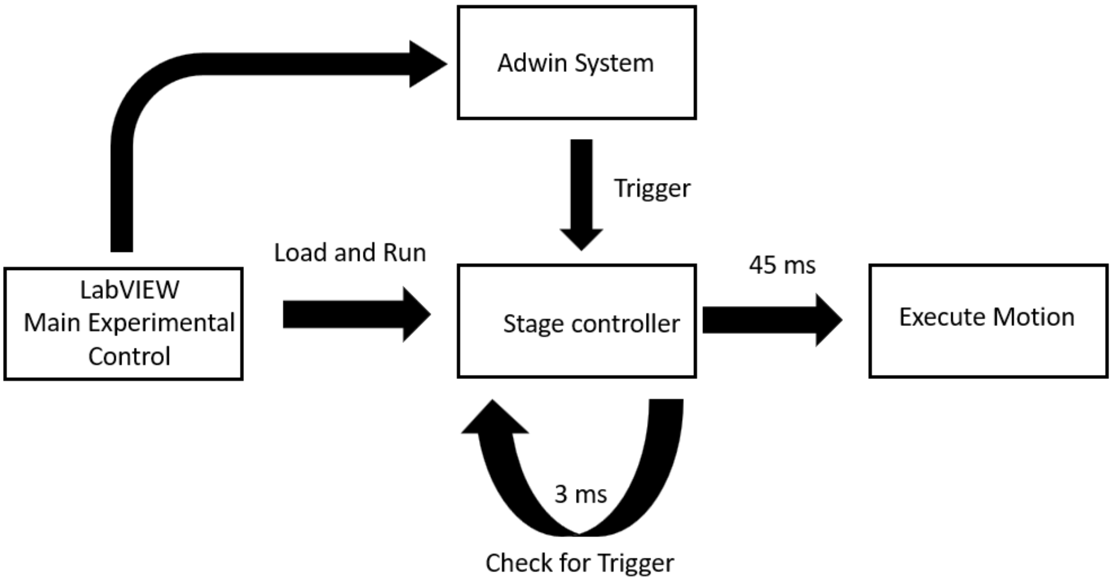

Figure 5.5: Flowchart of the real-time programming system

20 ms to be ready to detect the next trigger. Data exchange between the iXC2 controller and the LabVIEW is performed by reading and writing in text files in the controller. LabVIEW writes two text files to the iXC2 controller at the start, one which enables the controller and the other with all the motion parameters. When the LabVIEW run is terminated, it disables the Aeroscript code and ends execution.

5.4 Optimization of Transport Parameters

Optimising the transport parameters is required to minimise heating up to atoms in the trap and maximise the number of atoms reaching the science cell. The most important transport parameters we can tune are

1. Maximum speed of motion
2. Total time of motion
3. Ramp time and type

The start and stop positions of the motion are fixed for the motion. Ramp time is the time taken from rest to reach the maximum speed from rest. The total time of motion includes the ramp-up and ramp-down times and a constant speed section for the rest of the motion.

$$t_{total} = 2t_{ramp} + t_{cs} \tag{5.1}$$

Where t_{cs} is the time in the constant speed section.

5.4.1 Ramp Types

This section discusses various acceleration ramps that can be used for transport. A suitable transport type must have low acceleration and jerk values to reduce the number of atoms lost during motion due to heating. Here three important types of acceleration ramps are discussed below.

Linear

The linear acceleration ramp is the most trivial ramp type in which the speed increases linearly to the peak value. The linear ramp has the lowest peak acceleration value to reach a particular speed value. The acceleration value instantaneously jumps to a non-zero value at the start of motion making the jerk infinite. So, this ramp is not preferred for transporting Dy atoms where low jerk values are necessary.

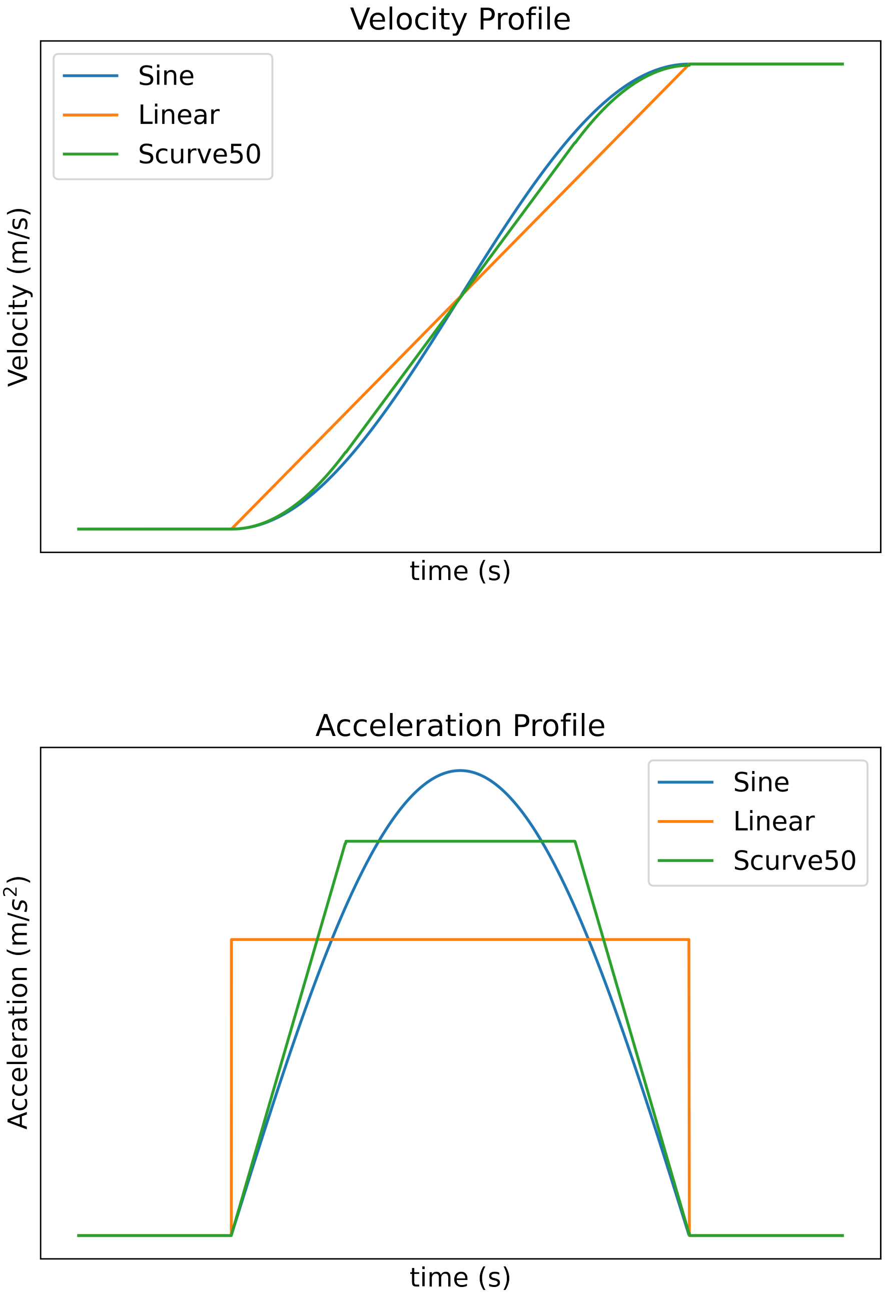

Figure 5.6: Velocity and Acceleration ramps for linear, sine and S-curve 50

Sinusoidal

A Sinusoidal or a half-Sine ramp follows a half cycle of a sine wave from $-\frac{\pi}{2}$ to $\frac{\pi}{2}$. This ramp follows a gradual increase and decrease in velocity and acceleration. The peak accelerations are higher than the linear ramp, but the jerk values are much lower.

S-Curve

S-Curve is a special ramp that incorporates constant acceleration and a constant jerk section. The peak acceleration and jerk values fall between the linear and sinusoidal ramps. The percentage of the constant acceleration section in the motion defines an S-Curve. An S-curve 50 means that 50% of the ramp has a constant acceleration, and 25% on each side is a constant jerk section. Changing the percentage of the linear section of the ramp helps us precisely control the jerk values as shown in 5.7. An S-curve 100 is the same as a linear ramp and has high jerk values.

5.4.2 Stage Motion

The Aeroscript program is used to program the motion of the stage with the different acceleration ramps discussed above. The program takes in the start position, ending position, ramp type, and constant speed section time and performs the motion upon the trigger. The stage is programmed to move from a starting to an ending position with the user-selected ramp type and speed. The program also records the motion at 1 ms intervals. Our objective is to transport atoms with different parameters to optimise the number of atoms transported. The Aeroscript program is run in ”CriticalSection” mode to dedicate the full processing power of the iXC2 controller for this single process. Previous works[26, 24] have achieved above 80% efficiency in transporting atoms using an air-bearing stage for alkali metal atom species.
Here, linear, sinusoidal and S-curve acceleration ramped motion is programmed in Aeroscript and executed on the ABL1500 stage, and the motion data is plotted in figure 5.8. The iXC2 controller records only the position of the stage, which is used to calculate the velocity and acceleration profiles by derivatives. This leads to a high amount of noise in the acceleration values calculated.

During the preparation of the thesis, the alignment of the dipole trap with the 1064 nm beam is ongoing. Transport data is expected as soon as the transport system is aligned and the building of science cell is completed.

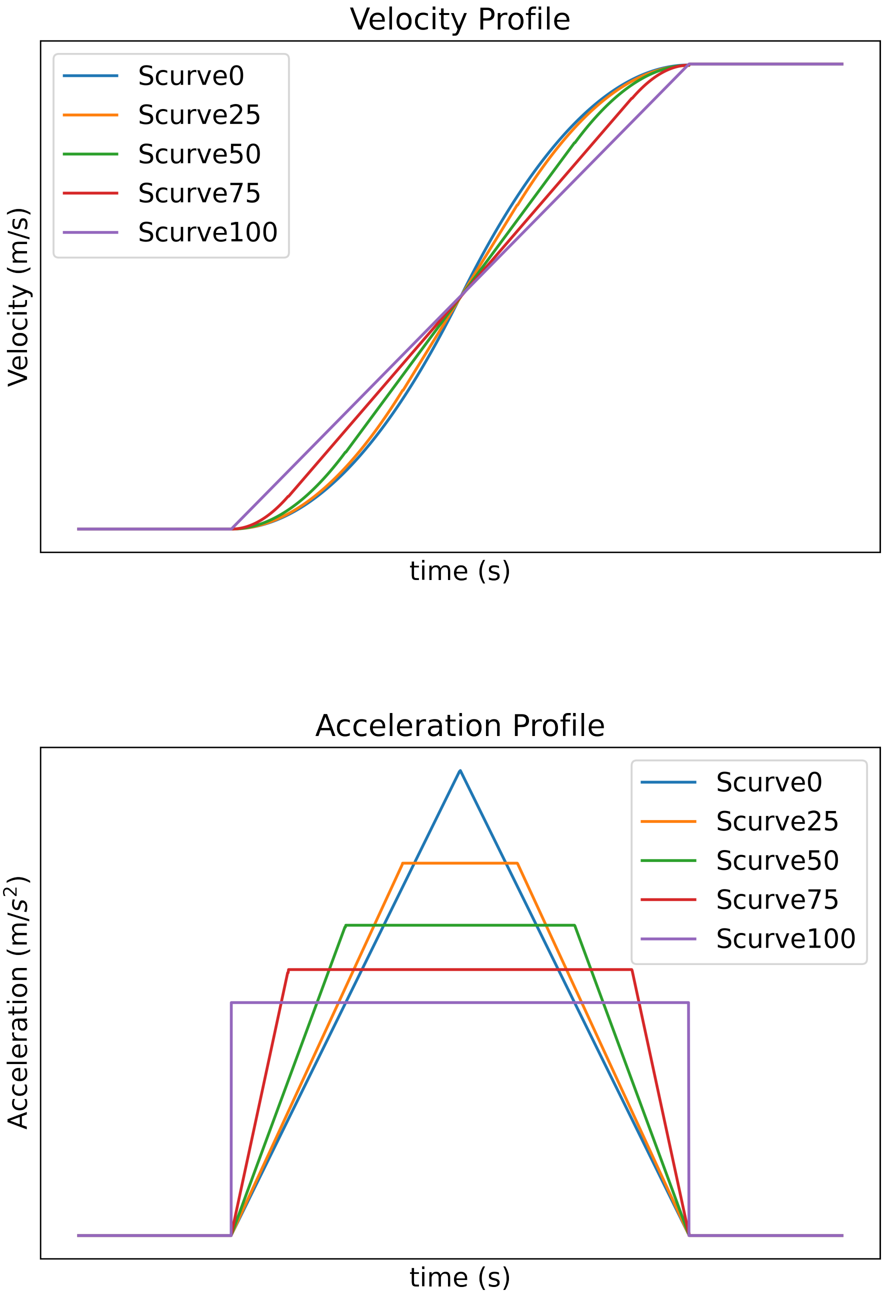

Figure 5.7: Velocity and Acceleration Ramps for various types of S-curves

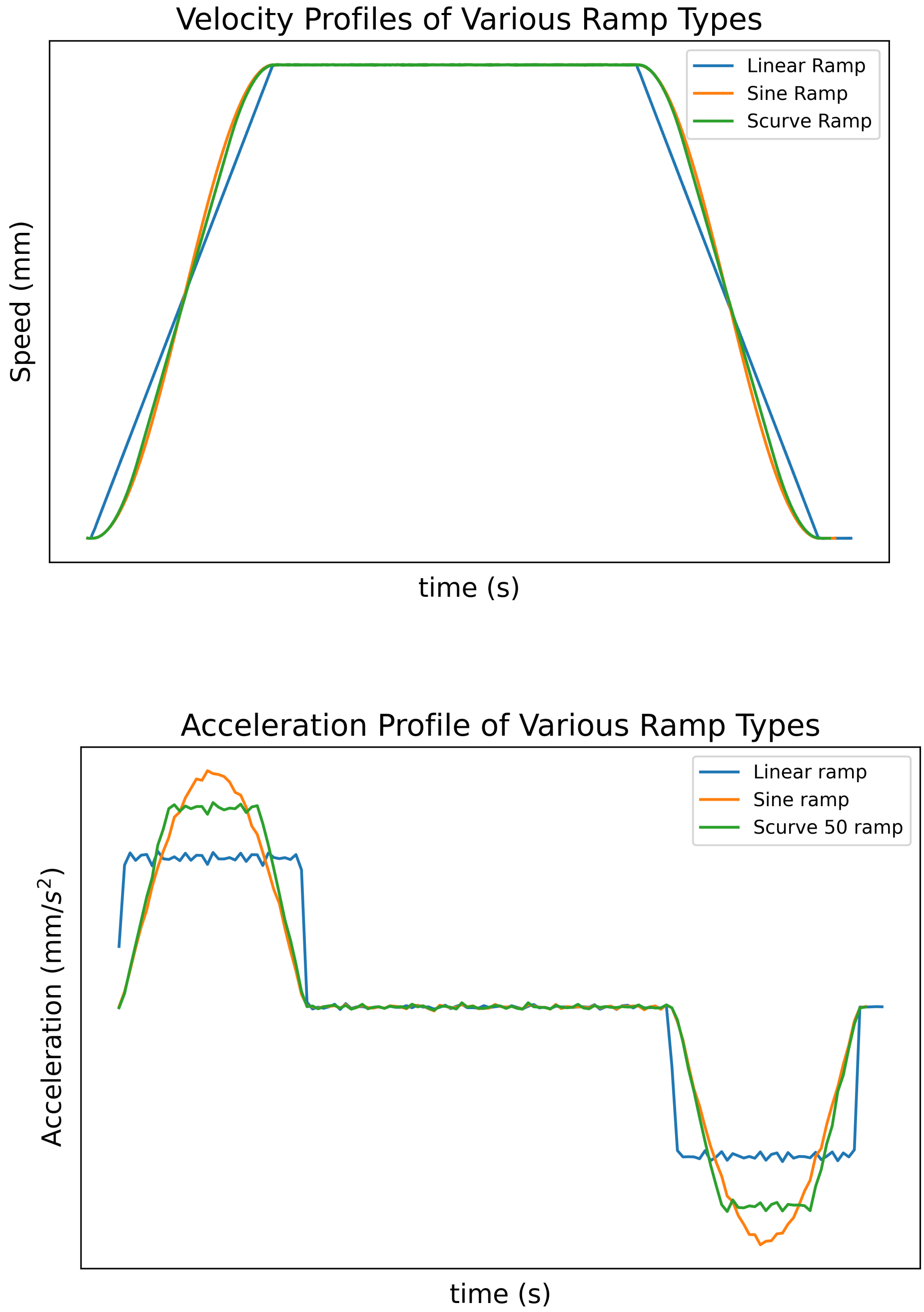

Figure 5.8: Various acceleration ramps implemented on ABL1500 stage

Chapter 6

Feshbach Coil Characterization

This chapter discusses designing and building a Helmholtz coils system to investigate the Feshbach resonances in Dysprosium.

6.1 Design of the Coils

A pair of coils in Helmholtz condition is used to create a uniform region of a magnetic field in a volume. For a single current loop, the Helmholtz condition is satisfied when the loop radius equals the separation distance. The Feshbach resonance measurements require up to 40 G, which is not achievable by a single loop. For coils with multiple windings, the Helmholtz condition is not straightforward. To design a pair of coils that can generate up to 40 G without heating up over the volume of the science cell, we use the Magpylib package in python. A magnetic field simulation is performed, varying the radius of the coils and the number of windings to get a configuration with a maximally uniform magnetic field at the centre. We use flat wires of dimensions 1 mm $\times$ 3 mm instead of round wires for maximum heat dissipation at high currents during operation. According to the AWG chart, these wires can carry up to 20 A of current. The calculated magnetic field of the final chosen configuration at 2 A current is plotted in figure 6.1.

The optimum configuration chosen from the simulation has a 30 mm long region of a uniform magnetic field along the axis. This configuration needs six layers of windings and eight in each layer, with forty-eight windings in total. With this configuration finalised, a holder is built to wind the wires on. This holder is made using aluminium to help in heat dissipation due to its large thermal conductivity. The coil holders are designed using the 3D design software Inventor to fit symmetrically around the science cell. The CAD design of the Feshbach coil holders with the windings is shown in figure 6.2.

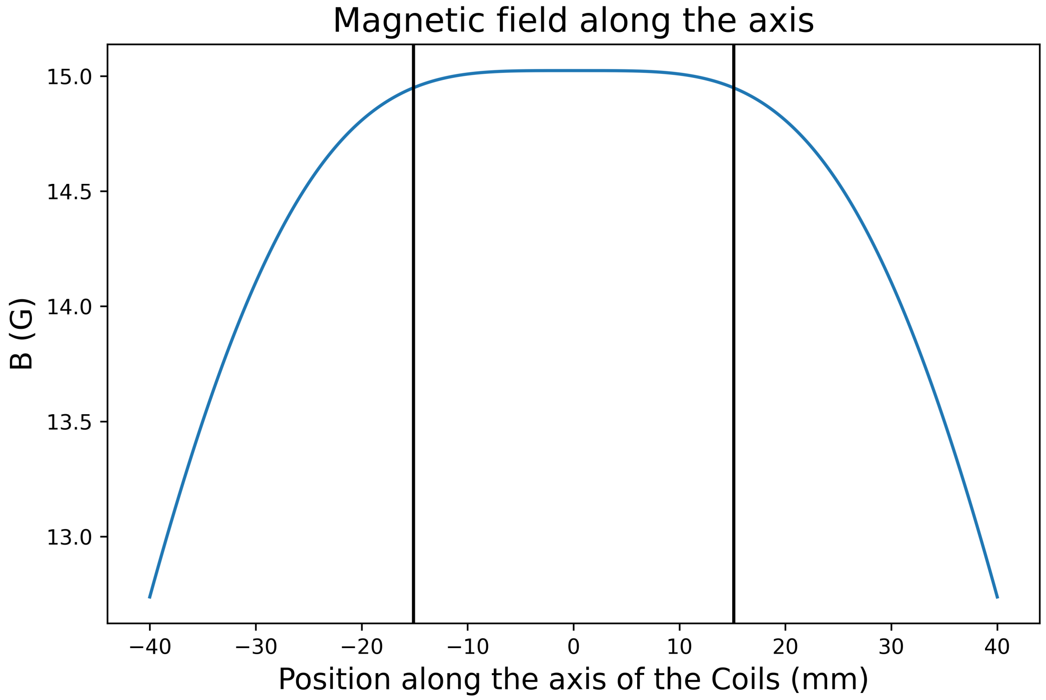

Figure 6.1: Calculated magnetic field along the axis of the coils

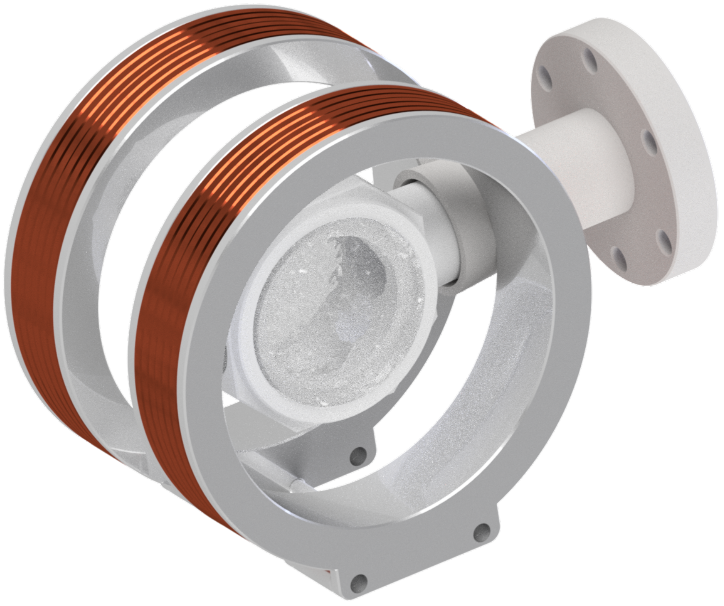

Figure 6.2: Feshbach Coil holders with the Science Cell

6.2 Magnetic Field Profile

The next step after designing and building the coils is characterising the performance. A Fluxgate magnetic field sensor is used to measure the magnetic field. This hall sensor can detect up to 3 G in either direction. The magnetic field variation measurement along the axis will tell us how accurate our simulation was. In figure 6.3, we can observe a 30 mm uniform region at the centre as predicted by the simulation.

Since we are limited by the measurement limit of the hall sensor, we will measure the magnetic field for higher currents by aligning it 86.6 ±0.2°away from its direction. This ensures that the sensor only detects a fraction of the magnetic field, allowing the measurement of magnetic fields due to higher currents. According to the simulation, the relation between the magnetic field and current is given by $B = 7.5I$. In figure 6.4, we plot the result of the magnetic field measurement as a function of current. The linear fit gives

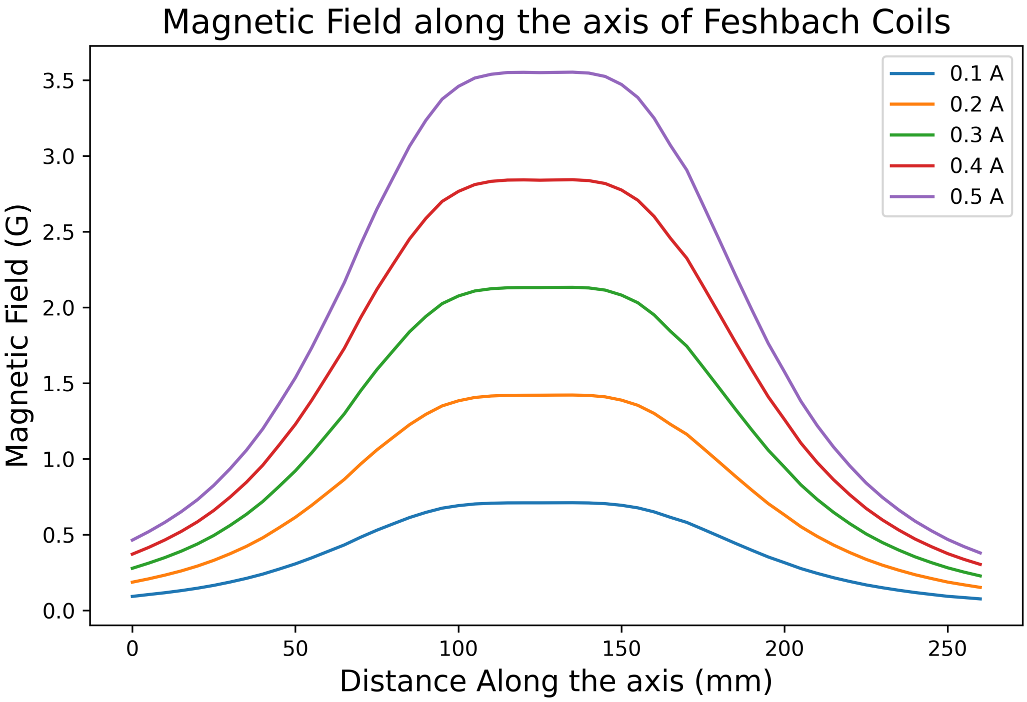

Figure 6.3: Feshbach Coil holders with the Science Cell

$$B = 7.10300 \times I + 0.00017 \tag{6.1}$$

Where the magnetic field B is in gauss, and I is in ampere.

As discussed in the theoretical section, we need a stable and high-resolution magnetic field for Feshbach resonance measurements. We use Rohde & Schwarz NGU401 source measurement unit as the current supply. It has a current output in the

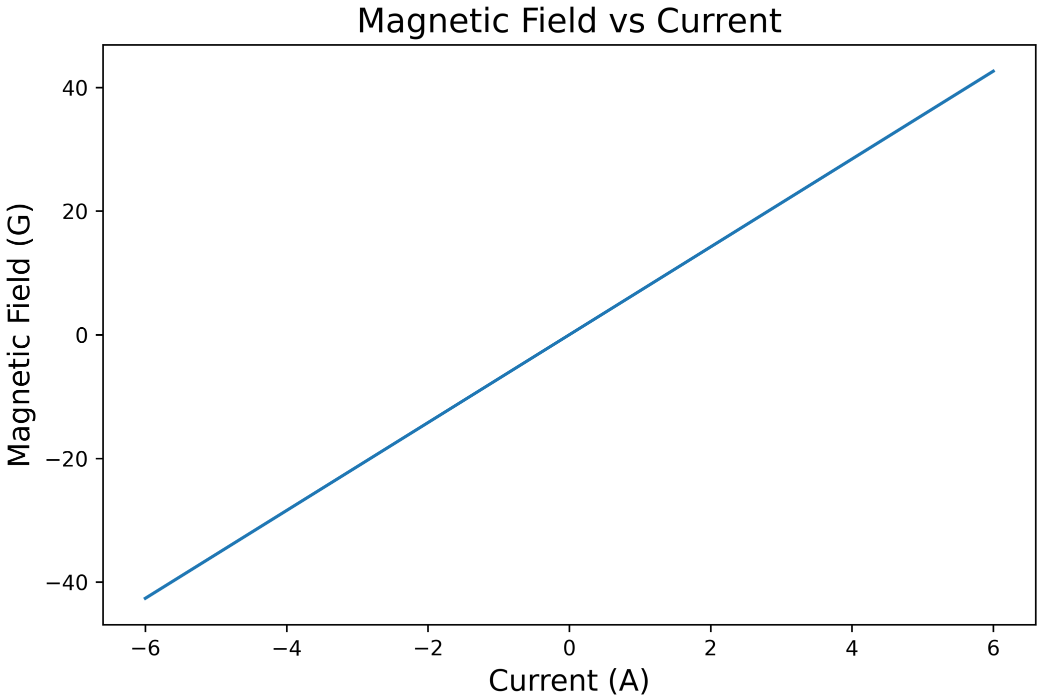

Figure 6.4: Magnetic field at the centre of the coils vs current

range of -10 A to 10 A with a resolution of 50 μA. With this resolution, we can resolve 0.36mG in the magnetic field. Noise measurement in the magnetic field is performed to determine how much noise is present in the current output. The noise figure is determined by taking the standard deviation of the magnetic field in a 10s period using an oscilloscope.The results are given in table 6.1.

Current (A)	Magnetic Field (G)	Noise (mG)
0.1	0.4925	6.8
0.2	2.6427	7.7
0.3	4.7532	31
0.4	6.8296	27
0.5	8.9786	25
0.6	11.1130	33

Table 6.1: Noise in the magnetic field produced by Feshbach Coils

We see that even though the noise is less than 1% of the magnetic field, the absolute value of the noise is larger than the smallest values of the width of Feshbach resonances in Dy. So, this power supply can resolve the Feshbach resonances with widths much larger than these noise values but not smaller ones.

6.3 Magnetic Field Switching Behaviour

While performing an atom loss spectroscopy measurement to determine the Dy cloud's Feshbach spectrum, fast magnetic field switching is necessary. This section discusses the delay in switching ON and OFF the magnetic field. Since the coils are inductors, they oppose any sudden change in the current due to the self and mutual induction of the coils. This leads to a delay in switching the magnetic fields ON and OFF. The switching ON delay is measured to be 4.06 ms, and the switching OFF delay is 5.12 ms. These delay times are large because of the 48 windings in each coil, thus increasing its self-induction. In addition, the close proximity of these large numbers of windings results in large mutual induction contributions.

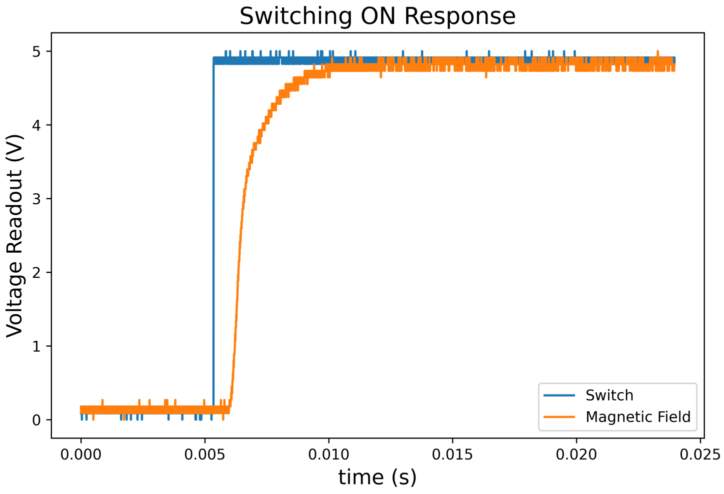

Figure 6.5: Magnetic field switch ON response

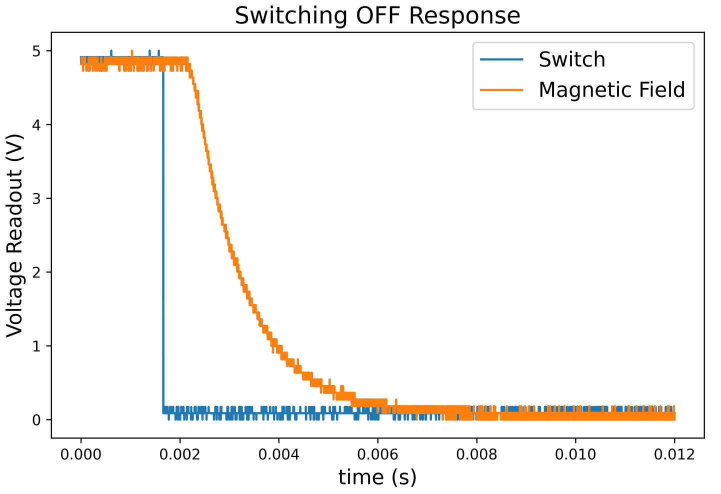

Figure 6.6: Magnetic field switch OFF response

Chapter 7

Summary and Outlook

7.1 Summary

The main goal of this work was the creation of a dense sample of a dipolar quantum gas of Dy and studying the collective effects. For this purpose, we designed and built an optical transport system to move Dy atoms into a home-built science cell with high optical access. designed and characterised a magnetic field system to precisely tune the contact interactions in Dy.
The science cell was built using a ceramic called Macor. The seven windows are made from UV-fused silica to withstand high-power lasers and high temperatures. We tested various low-outgassing epoxies to build the science cell to get a vacuum in the order of 10^{-10} mbar. We optimised the curing and baking-out temperatures for the lowest leakage rates and the highest vacuum. A leakage rate of $\leq 10^{-11}$ mbarL/s and a vacuum of 5.28×10^{-10} mbar is obtained when epoxy A is cured at 80°C for 640 minutes with a heating up and cooling down rate of 0.25°C per minute.

After deciding the epoxies for the construction of the science cell, we moved on to the setup of the optical transport of the atoms to the science cell. The atoms initially cooled and trapped in an MOT using the 626 nm transition. The transport system has to load the atoms from the MOT to an ODT and then drag it to the science cell to be re-trapped in microscopic ODT. The transport is carried out by a programmable high-precision air-bearing Aerotech translation stage. The stage is programmed and integrated into the previously existing LabVIEW experimental control. The stage is programmed in a real-time style to minimise shot-to-shot variation and execute any user-defined ramps from the LabVIEW interface. Three acceleration ramps are primarily considered to optimise the transport: linear, sine and s-curve. The efficiency of the transport is determined by the number of atoms transported to the science cell.

An ideal transport should have low acceleration and jerks during the motion to prevent atoms from heating up and escaping the trap. The alignment of the transport optical dipole trap is still ongoing during the preparation of this thesis.

Once the atoms are transported to the science cell and are re-trapped in a microscopic ODT, we tune the contact interactions and investigate the scattering properties using Feshbach resonances. A highly precise magnetic field system is built using pair of Helmholtz coils to provide a uniform magnetic field in a 30 mm region at the centre of the science cell. The pair of Helmholtz coils are built and characterised to establish the magnetic field at the centre vs current. The measured magnetic field is shown to be very close to the predictions from the simulations. Finally, the switching behaviour of the magnetic field is measured. The switch ON delay is 4.06 ms, and the switch OFF delay is 5.12 ms. In addition, the magnetic field noise is measured to be larger than the width of the smaller Feshbach resonances in reported spectra of Dysprosium, making the power supply unsuitable for resolving smaller resonances.

7.2 Future Plan

The octagonal science cell will be prepared using epoxy A to fix the UV-fused silica windows and titanium flange with optimised curing temperature and heating and cooling ramp rates. This completed octagonal science cell will be tested and attached to the MOT chamber with an ion pump and pressure sensor. The transport setup will be completed with the mirrors mounted on the translation stage, and acceleration ramps will be tested to maximise atom transport efficiency. The transported atoms are re-trapped in a microscopic ODT to achieve higher densities to investigate collective effects. The Feshbach spectra of the dense Dy atom sample are mapped using atom loss spectroscopy at the temperatures achieved. The spectrum is then used to precisely tune the contact interactions in the cloud to obtain different molecular bound states in Dy. The power supply can be improved to reduce the noise in the magnetic field below 5 mG using active compensation in the output current. Such a low-noise magnetic field source will allow resolving even the smallest reported Dy Feshbach resonances in literature.

Appendix A

AeroScipt Code for Transport

```
//Global Variables
var $NumberofSamplesPerSecond as integer = 1000
var $DataSaveFile as string = "/MotionPositionAndSpeed/Iteration "
var $MaxIteration as integer = 10
var $EnableFile as string = "/MotionData/MotionEnable.txt"
var $Iteration as integer = 1
var $CheckMilestone as integer = 1000
var $t1, $t2 as real

program
  Enable(X)
  Home(X)
  var $MotionInfo as handle
  var $Start, $End, $RampTime, $ContinuousSpeedTime as real
  var $AccelerationRampType as integer

  while (Enable())
    $MotionInfo = FileOpenText("/MotionData/MotionInfo.txt", FileMode.Read)


    var $FileData as string
    $FileData = FileTextReadLine($MotionInfo)
    $Start = StringToReal($FileData)
    $FileData = FileTextReadLine($MotionInfo)
    $End = StringToReal($FileData)
    $FileData = FileTextReadLine($MotionInfo)
    $RampTime = StringToReal($FileData)
    $FileData = FileTextReadLine($MotionInfo)
```

```
    $ContinuousSpeedTime = StringToReal($FileData)
    $FileData = FileTextReadLine($MotionInfo)
    var $OperationMode as integer = StringToInteger($FileData)
    $FileData = FileTextReadLine($MotionInfo)
    $AccelerationRampType = StringToInteger($FileData)
    FileClose($MotionInfo)


    var $PeakSpeed as real = ($End - $Start) / ($RampTime +
        $ContinuousSpeedTime)
    var $Stop1, $Stop2 as real
    var $TotalTime as real = 2 * $RampTime + $ContinuousSpeedTime
    var $RecordTime as real = 1.5 * $TotalTime
    $Stop1 = $Start + 0.5 * $PeakSpeed * $RampTime
    $Stop2 = $Stop1 + $PeakSpeed * $ContinuousSpeedTime
    SetupTaskTargetMode(TargetMode.Absolute)
    switch ($AccelerationRampType)
      case 0
        SetupCoordinatedRampType(RampType.Linear)
      case 1
        SetupCoordinatedRampType(RampType.Sine)
      case 2
        SetupCoordinatedRampType(RampType.SCurve)
      default
        SetupCoordinatedRampType(RampType.Linear)
    end
    switch ($OperationMode)
      case 0
        TransportToScienceCellI($Start, $End, $PeakSpeed, $RecordTime,
            $RampTime)
      case 1
        TransportInsideMOT($Start, $End, $PeakSpeed, 2 * $RecordTime,
            $RampTime, 2 * $TotalTime)
    end
  end
  Home(X)
  Disable(X)
end

function TransportToScienceCellI($Start as real, $End as real, $PeakSpeed as
    real ,$RecordTime as real, $RampTime as real)
```

```
   var $CheckNum as integer
   SetupCoordinatedRampValue(RampMode.Time, $RampTime)
   var $filename as string
   var $IterationData as handle
   $CheckNum= 0
   MoveLinear(X, $Start, $PeakSpeed)
   $filename = $DataSaveFile + IntegerToString($Iteration) + ".dat"
   DataCollectionReset()
   DataCollectionAddSystemSignal(SystemDataSignal.DataCollectionSampleTime)
   DataCollectionAddAxisSignal(X, AxisDataSignal.PositionFeedback)
   DataCollectionAddAxisSignal(X, AxisDataSignal.VelocityFeedback)
   DataCollectionAddTaskSignal(1, TaskDataSignal.TaskState)
   while ($CheckNum < $CheckMilestone)
      $CheckNum++
      $t1 = StatusGetSystemItem(51)
      switch (DigitalInputGet(X, 0))
         case 1
            CriticalSectionStart()
            DataCollectionStart($filename, Ceil($NumberofSamplesPerSecond *
                $RecordTime), 1)
            while (StatusGetSystemItem(51) - $t1 < 45)
               continue
            end
            $t2 = StatusGetSystemItem(51)
            MoveLinear(X, $End, $PeakSpeed)
            WaitForInPosition(X)
            DataCollectionStop()
            CriticalSectionEnd()
            $IterationData = FileOpenText("/MotionData/MotionIteration.txt",
                FileMode.Overwrite)
            FileTextWriteString($IterationData, $filename)
            FileClose($IterationData)
            $Iteration++
            AppMessageDisplay("Difference: " + RealToString($t2 - $t1) + " t1:
                " + RealToString($t1) + " t2: " + RealToString($t2))
            break
      end
   end

end
```

```
function TransportInsideMOT($Start as real, $End as real, $PeakSpeed as real
    ,$RecordTime as real, $RampTime as real, $TotalTime as real)
   var $CheckNum as integer = 0
   SetupCoordinatedRampValue(RampMode.Time, $RampTime)
   var $filename as string
   var $IterationData as handle
   MoveLinear(X, $Start, $PeakSpeed)
   $filename = $DataSaveFile + IntegerToString($Iteration) + ".dat"
   DataCollectionReset()
   DataCollectionAddSystemSignal(SystemDataSignal.DataCollectionSampleTime)
   DataCollectionAddAxisSignal(X, AxisDataSignal.PositionFeedback)
   DataCollectionAddAxisSignal(X, AxisDataSignal.VelocityFeedback)
   DataCollectionAddTaskSignal(1, TaskDataSignal.TaskState)
   while ($CheckNum < $CheckMilestone)
      $CheckNum++
      $t1 = StatusGetSystemItem(51)
      switch (DigitalInputGet(X, 0))
         case 1
            CriticalSectionStart()

            DataCollectionStart($filename, Ceil($NumberofSamplesPerSecond *
                $RecordTime), 1)
            while (StatusGetSystemItem(51) - $t1 < 45)
               continue
            end
            $t2 = StatusGetSystemItem(51)
            MoveLinear(X, $End, $PeakSpeed)
            MoveLinear(X, $Start, $PeakSpeed)
            WaitForInPosition(X)
            DataCollectionStop()
            CriticalSectionEnd()
            $IterationData = FileOpenText("/MotionData/MotionIteration.txt",
                FileMode.Overwrite)
            FileTextWriteString($IterationData, $filename)
            FileClose($IterationData)
            $Iteration++
            AppMessageDisplay("Difference: " + RealToString($t2 - $t1) + " t1:
                " + RealToString($t1) + " t2: " + RealToString($t2))
            break
      end
```

```
   end

end




function Enable() as integer
   var $MotionEnable as handle = FileOpenText($EnableFile, FileMode.Read)
   var $Enable as integer = StringToInteger(FileTextReadLine($MotionEnable))
   FileClose($MotionEnable)
   return $Enable
end
```

Bibliography

[1] R. H. Dicke. “Coherence in Spontaneous Radiation Processes”. In: *Phys. Rev.* 93 (1 1954), pp. 99–110. DOI: `10.1103/PhysRev.93.99`. URL: `https://link.aps.org/doi/10.1103/PhysRev.93.99`.

[2] R. H. Dicke. “Coherence in Spontaneous Radiation Processes”. In: *Phys. Rev.* 93 (1 1954), pp. 99–110. DOI: `10.1103/PhysRev.93.99`. URL: `https://link.aps.org/doi/10.1103/PhysRev.93.99`.

[3] A. Griesmaier, J. Stuhler, and T. Pfau. “Production of a chromium Bose–Einstein condensate”. In: *Applied Physics B* 82.2 (2005), pp. 211–216. DOI: `10.1007/s00340-005-2070-4`. URL: `https://doi.org/10.1007%5C%2Fs00340-005-2070-4`.

[4] Thierry Lahaye et al. “Strong dipolar effects in a quantum ferrofluid”. In: *Nature* 448.7154 (2007), pp. 672–675. ISSN: 1476-4687. DOI: `10.1038/nature06036`. URL: `https://doi.org/10.1038/nature06036`.

[5] Mingwu Lu et al. “Strongly Dipolar Bose-Einstein Condensate of Dysprosium”. In: *Physical Review Letters* 107.19 (2011). DOI: `10.1103/physrevlett.107.190401`. URL: `https://doi.org/10.1103%5C%2Fphysrevlett.107.190401`.

[6] K. Aikawa et al. “Bose-Einstein Condensation of Erbium”. In: *Physical Review Letters* 108.21 (2012). DOI: `10.1103/physrevlett.108.210401`. URL: `https://doi.org/10.1103%5C%2Fphysrevlett.108.210401`.

[7] Kristian Baumann et al. “Observation of low-field Fano-Feshbach resonances in ultracold gases of dysprosium”. In: *Physical Review A* 89.2 (2014). DOI: `10.1103/physreva.89.020701`. URL: `https://doi.org/10.1103%5C%2Fphysreva.89.020701`.

[8] T. Maier et al. “Emergence of Chaotic Scattering in Ultracold Er and Dy”. In: *Phys. Rev. X* 5 (4 2015), p. 041029. DOI: `10.1103/PhysRevX.5.041029`. URL: `https://link.aps.org/doi/10.1103/PhysRevX.5.041029`.

[9] Dieter Meschede. *Optics, Light, and Lasers: The Practical Approach to Modern Aspects of Photonics and Laser Physics*. Wiley, 2004.

[10] Rudolf Grimm, Matthias Weidemüller, and Yurii B. Ovchinnikov. “Optical Dipole Traps For Neutral Atoms”. In: (1999). arXiv: `physics/9902072 [physics.atom-ph]`.

[11] Simon Baier. “An optical dipole trap for Erbium with tunable geometry”. PhD thesis. 2012.

[12] Cheng Chin et al. “Feshbach resonances in ultracold gases”. In: *Rev. Mod. Phys.* 82 (2 2010), pp. 1225–1286. DOI: `10.1103/RevModPhys.82.1225`. URL: `https://link.aps.org/doi/10.1103/RevModPhys.82.1225`.

[13] Niels Syassen. “Interacting Feshbach Molecules”. PhD thesis. 2008. URL: `https://www.mpq.mpg.de/5723445/MPQ319.pdf`.

[14] A. J. Moerdijk, B. J. Verhaar, and A. Axelsson. “Resonances in ultracold collisions of ^{6}Li, ^{7}Li, and ^{23}Na”. In: *Phys. Rev. A* 51 (6 1995), pp. 4852–4861. DOI: `10.1103/PhysRevA.51.4852`. URL: `https://link.aps.org/doi/10.1103/PhysRevA.51.4852`.

[15] E. Lucioni et al. “Dysprosium dipolar Bose-Einstein condensate with broad Feshbach resonances”. In: *Phys. Rev. A* 97 (6 2018), p. 060701. DOI: `10.1103/PhysRevA.97.060701`. URL: `https://link.aps.org/doi/10.1103/PhysRevA.97.060701`.

[16] Thomas Maier. “Interactions in a Quantum Gas of Dysprosium Atoms”. PhD thesis. 2015.

[17] Kristian Baumann et al. “Observation of low-field Fano-Feshbach resonances in ultracold gases of dysprosium”. In: *Physical Review A* 89.2 (Feb. 2014). DOI: `10.1103/physreva.89.020701`. URL: `https://doi.org/10.1103%5C%2Fphysreva.89.020701`.

[18] T Lahaye et al. “The physics of dipolar bosonic quantum gases”. In: *Reports on Progress in Physics* 72.12 (2009), p. 126401. DOI: `10.1088/0034-4885/72/12/126401`. URL: `https://doi.org/10.48550/arXiv.0905.0386`.

[19] Carina Baumgärtner. “Laser Cooling of Dysprosium”. MA thesis. Mainz, Germany: Johannes Gutenberg University, 2017.

[20] Dimitra Cristea. MA thesis. Mainz, Germany: Johannes Gutenberg University, 2023.

[21] D. Schrader et al. “An optical conveyor belt for single neutral atoms”. In: *Applied Physics B* 73.8 (2001), pp. 819–824. DOI: `10.1007/s003400100722`. URL: `https://doi.org/10.1007%5C%2Fs003400100722`.

[22] Sascha H. Hauck, Gernot Alber, and Vladimir M. Stojanovi ć. “Single-atom transport in optical conveyor belts: Enhanced shortcuts-to-adiabaticity approach”. In: *Phys. Rev. A* 104 (5 2021), p. 053110. DOI: `10.1103/PhysRevA.104.053110`. URL: `https://link.aps.org/doi/10.1103/PhysRevA.104.053110`.

[23] Julian Lé onard et al. “Optical transport and manipulation of an ultracold atomic cloud using focus-tunable lenses”. In: *New Journal of Physics* 16.9 (2014), p. 093028. DOI: `10.1088/1367-2630/16/9/093028`. URL: `https://doi.org/10.1088%5C%2F1367-2630%5C%2F16%5C%2F9%5C%2F093028`.

[24] T. L. Gustavson et al. “Transport of Bose-Einstein Condensates with Optical Tweezers”. In: *Phys. Rev. Lett.* 88 (2 2001), p. 020401. DOI: `10.1103/PhysRevLett.88.020401`. URL: `https://link.aps.org/doi/10.1103/PhysRevLett.88.020401`.

[25] Christoph M. Kirsch. “Principles of Real-Time Programming”. In: (). URL: `https://cs.uni-salzburg.at/~ck/publications/invited/EMSOFT02-PrinciplesRTProgramming.pdf`.

[26] Ahmed Omran. “A Microscope for Fermi Gases”. PhD thesis. 2016. URL: `https://d-nb.info/1102157236/34`.